Study of the doubly charged Higgs boson single production using lepton parton distribution functions with the ATLAS detector

Daniel Magdalinski

Thesis submitted for the degree of Master of Science
Project duration: 10 months-fulltime
Supervised by Else Lytken

LUND UNIVERSITY

Department of Physics
Division of Particle Physics
Lund University
HT 2021-VT 2022

Abstract

Searches for the doubly charged Higgs($H^{\pm\pm}$) aim to find evidence for models that could explain the origin of neutrino masses. Earlier searches at the LHC have used different production processes for the $H^{\pm\pm}$, with the recent development of lepton parton distribution functions new leptonic production processes are able to be studied. In this thesis the single production process $\ell^{\pm} + \ell^{\pm} \rightarrow H^{\pm\pm}$ has been studied together with its subsequent decay back into charged leptons. The final state of two prompt and isolated same-sign charged leptons is rare at the LHC and is therefore a powerful probe that this thesis will focus on. The triggering, reconstruction and selection of charged leptons at ATLAS Run 2 have been analyzed to give a final estimate of the number of events that could be detected at Run 2, 3 and 4. The final events dependence on model parameters have also been investigated with large differences in cross section. Finally, several improvements to be made for a full analysis is discussed.

Nomenclature

Abberiations	Meaning	Symbols	Meaning
DCH	Doubly Charged Higgs	e	electron
SM	Standard Model	μ	muon
PDF	Parton Distribution Function	τ	tauon
QED	Quantum Electro Dynamics	u	up quark
QCD	Quantum Chromo Dynamics	d	down quark
LHC	Large Hadron Collider	c	charm quark
ATLAS	A Toroidal LHC ApparatuS	s	strange quark
CMS	Compact Muon Solenoid	t	top quark
ALICE	A Large Ion Collider Experiment	b	bottom quark
LHCb	LHC beauty	$H^{\pm\pm}$	Doubly charged Higgs boson
CERN	Conseil Européen pour la Recherch Nucléaire	h	Higgs boson
ID	Inner Detector	W	W boson
SCT	Silicon miCrosTrip	Z	Z boson
TRT	Transition Radiation Tracker	γ	photon
ECal	Electromagnetic Calorimeter	g	gluon
lAr	liquid Argon	$\sqrt{s}$	Center of mass energy
HCal	Hadronic Calorimiter	σ	Cross section
MS	Muon Spectrometer	L	Luminosity
MDT	Monitored Drift Tubes	L_{int}	Integrated luminosity
CSC	Cathode Strip Chambers	p_T	Transverse momentum
RPC	Resistive Plate Chambers	η	Pseudorapidity
TGC	Thin Gap Chambers	ϕ	Azimuthal angle
HLT	High-Level Trigger	$\Delta\phi$	Azimuthal separation
RoI	Regions of Interest	ΔR	Angular separation
MC	Monte Carlo	l	lepton
LO	Leading Order	m	mass
NLO	Next-to Leading Order	d_0	Impact parameter
		Δz_0	Longitudinal impact parameter
		ν_D	Triplet vacuum expectation value

Table of contents

Chapter 1

Introduction

The aim of particle physics is to describe the fundamental form of matter and its interactions. In the last 70 years the development of theory and many discoveries of several fundamental particles have led to the Standard Model(SM). The SM describes the fundamental particles and their interactions with each other. It is a very successful model but there are still questions that it cannot answer. Some of these are, the missing description of the fourth force: gravity, dark matter, dark energy, matter-antimatter asymmetry and the nature of neutrino masses. This thesis will focus on a particle theorised by an extension of the SM that explains neutrino masses.

The Large Hadron Collider(LHC)[1] is the largest particle collider in the world located on the French-Swish border outside of Geneva. The LHC accelerates protons up to $\sqrt{s} = 14$ TeV in a two-ring superconducting collider tunnel with a 26.7 km circumference. The ATLAS experiment[2] is a multi-purpose experiment designed to probe a wide range of new physics and to perform precision measurements of SM processes at the LHC. After the discovery of the Higgs boson[3], the detector is focused on several Beyond the SM(BSM) signatures such as supersymmetry, top quark properties, CP violation and dark matter. The detector setup is segmented in a layered design with four distinct layers optimized to reconstruct several different fundamental particles.

The Doubly Charged Higgs(DCH) $H^{\pm\pm}$ is a gauge boson proposed in several BSM theories, such as left-right symmetric models[4, 5, 6], type-II seesaw models[7], 3-3-1 models[8], Zee-Babu neutrino model[9, 10] and the Georgi-Machacek model[11]. In this thesis, the type-II seesaw model was used to generate the DCH. This model introduces a SU(2) Higgs triplet Δ to the SM, which gives rise to four new bosons Δ^0, χ, $H^{\pm}$ and $H^{\pm\pm}$. The DCH can decay into W bosons and charged leptons, where the decay is heavily dependent on the Δ triplet vacuum expectation value: ν_Δ. In this thesis the focus is on the charged lepton decay scenario and therefore ν_Δ is forced to be smaller than 10^{-4}. Previous searches of the DCH at ATLAS[12] have focused on the more common double production $p + p \to H^{\pm\pm} + H^{\mp\mp}$ through neutral current, photon, vector boson and gluon fusion. In this thesis recently calculated lepton parton distribution functions(PDF) [13] are implemented to produce the DCH. This enables single production of the DCH: $\ell^{\pm} + \ell^{\pm} \to H^{\pm\pm}$, which could potentially be a cleaner signature

to detect at ATLAS. The aim of this thesis is to perform an estimation of the number of these events that could be observed with the ATLAS detector during Run 2, 3 and 4 of the LHC.

The thesis is organized in different Chapters. In Chapter 2 the theoretical background of the SM, DCH and lepton PDFs is described together with the experimental background of the LHC and the ATLAS detector. Chapter 3 describes the simulation of data and some characteristics of the signal. In Chapter 4 the cuts, selections, triggers and uncertainties of the overall event reconstruction are explained. The final results of the thesis will be detailed in Chapter 5. Finally, the summary and conclusion of the thesis is given in Chapter 6.

Chapter 2

Theory and background

2.1 The Standard Model

The Standard Model of particle physics is the current model describing what we know about the fundamental interactions of the Universe. The model consists of 17 elementary particles, which are divided into two main groups: fermions and bosons. The fermions can be further divided into leptons and quarks which together make up the visible matter. The bosons consist of the gauge bosons which act as the carrier of the fundamental forces and the Higgs boson which is the origin of mass in the model. The particles have an antiparticle counterpart which has the same mass but opposite electrical charge [14].

2.1.1 Fermions

Fermions have half integer spin and follow Fermi-Dirac statistics. Mainly, this means that they obey the Pauli exclusion principle stating that two indistinguishable fermions can not occupy the same quantum state.

The leptons consist of three families of doublets: electron, muon and tauon as well as their neutrino counterparts as can be seen in figure 2.1. The electron, muon and tauon have electric charge -e while the neutrinos are neutral. The neutrino does not gain its mass from the standard Higgs boson and currently the mechanism that gives mass to the neutrino as well as the value of their mass is unknown. The theory this thesis is looking into gives a mechanism for the mass of the neutrinos [16].

The quarks also consist of three families of doublets: up and down, charm and strange, top and bottom. As seen in figure 2.1 the top row of the quarks have electric charge $\frac{2}{3}e$ while the bottom row have electric charge $-\frac{1}{3}e$. The quarks carry a certain quantum number related to the strong force called color charge. There are three color charges and quarks can not be observed on their own, only while bound in a color neutral state. These compound states are called hadrons and the most common ones are the proton and neutron that make up the nucleus of the atom [16].

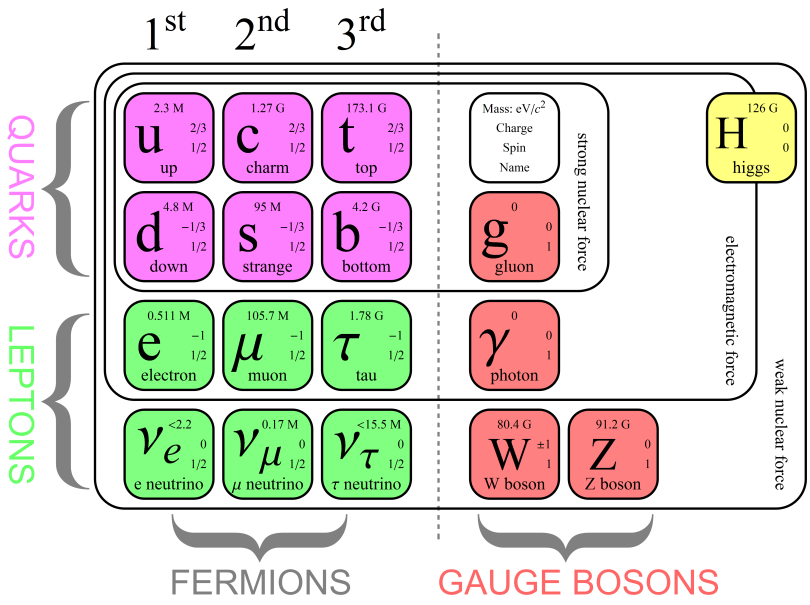

Figure 2.1: The standard model of elementary particles. [15]

2.1.2 Bosons and The Forces

From current understanding of physics there are four forces in nature: gravity, electromagnetism, the weak and strong interactions. The three forces excluding gravity are all included within the Standard Model and are mediated by the gauge bosons shown in figure 2.1 in red. Gravity is the oldest theory but is only understood classically through Newton and relativistically with Einstein but so far no quantized model has been constructed[17].

The combined electromagnetic force was first developed classically by Maxwell over a hundred years ago. Electromagnetism was the first theory to be quantized into QED(Quantum Electro Dynamics) by Tomonaga, Feynman, and Schwinger in the 1940s. QED is mediated by the photon. The photon is massless which means that the range of QED is in theory infinite but the strength of the force is reduced over distance by a factor of $1/d^2$. QED affects all the fermions except the neutrino which does not carry electric charge[17].

The weak nuclear force is mediated by the W and Z bosons. The theory was developed during the 50s and 60s which culminated in electroweak theory which combines the weak and electromagnetic force into a single force [17]. The force carriers of the weak force W and Z are massive, with masses around 80-90 times the mass of the proton. The high mass of the force carriers means that the force has a very short range. The weak force is the only force that can change lepton and quark flavour as well as violate parity and charge-parity symmetry. The weak force couples to all particles and is responsible for many radioactive decays in the form of β decay [14].

The strong nuclear force is mediated by the gluon that is massless and is described by Quantum Chromo Dynamics(QCD). Similar to electic charge in QED, particles in QCD carry color charge, with three different charges. As mentioned before quarks are the only fermions that carry color charge and therefore the only ones affected by the strong nuclear

force. An important property of QCD is that the gluon carries color and anti-color charge which leads to it being able to self-interact. The self-interaction of the force carrier leads to two fundamental properties of the force: color confinement and asymptotic freedom. Color confinement means that the force becomes stronger with increasing distance leading to the quarks being confined within hadrons. Asymptotic freedom means that the interactions gets weaker at shorter distances leading to the quarks behaving more like free particles[14].

2.1.3 The Higgs Boson

The most recent addition to the Standard Model is the scalar boson called the Higgs boson. This boson was discovered in 2012 by CMS[18] and ATLAS[3] independently. The Higgs boson was an important discovery and confirmed the theory of spontaneous symmetry breaking by Higgs, Englert & Brout and Guralnik et al., first theorized in 1964. QED and QCD do not explain how particles get their masses, in fact they are treated as massless within these theories. This was the main motivation for introducing a new scalar field now called the Higgs field. For other fields, such as the electromagnetic one, the potential is zero in the state where no particles are present also called the vacuum state. The potential of the Higgs field is shown in equation 2.1,

$$V(\eta) = \mu^2 \eta\eta^\dagger + \lambda(\eta\eta^\dagger)^2 \tag{2.1}$$

where λ and μ^2 are real parameters and η is the SU(2) Higgs field. Varying μ^2 while λ is required to be positive leads to the two cases shown in figure 2.2. For $\mu^2 > 0$ this is a normal second-degree equation but for $\mu^2 < 0$ the potential has a nonzero value ν in its vacuum state. This leads to a circle of minimum instead of a point. This form of the potential breaks the gauge invariance of the theory which leads to the the gauge bosons no longer being required to have zero mass [14]. This mechanism gives mass to the gauge bosons $W^\pm$ and Z^0 but not automatically to the fermions. With the Higgs field being a SU(2) field we can write an SU(2) interaction term with the SU(2) fermions. The current SM assumes that there are no

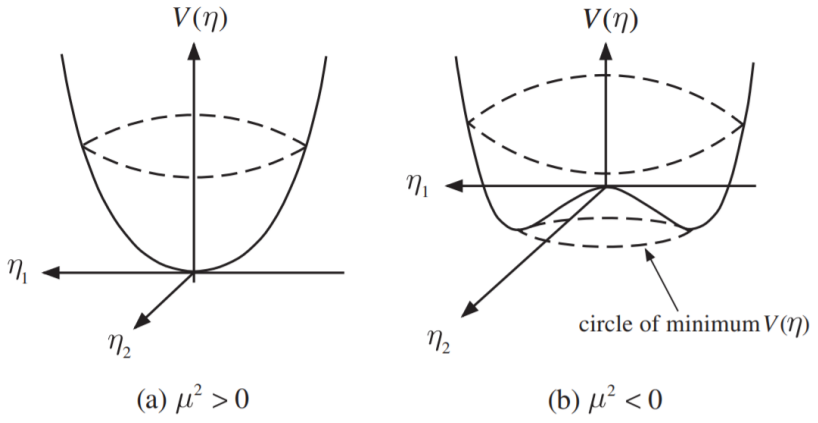

Figure 2.2: Potential energy density $V(\eta)$ as written in equation 2.1 with $\lambda > 0$. $\mu^2 > 0$ gives second degree equation, $\mu^2 < 0$ gives the Higgs potential.

right-handed neutrinos and in fact if they existed they would not interact electroweakly and therefore essentially be impossible to observe. This means that the Higgs does not give the neutrino its mass and this is still an open question to this day [16].

2.2 Doubly Charged Higgs

The SM has been very successful in describing and predicting the particles and their properties that have been observed at various experiments[19]. Despite of this, there exists a couple of questions that the SM cannot explain, one of these is the origin of the neutrino masses. One extensions of the SM that gives mass to the neutrinos is the type-II seesaw model[7, 20]. In this scenario the Higgs sector ϕ of the SM is extended by a SU(2) Higgs triplet Δ.

$$\Delta = \begin{pmatrix} \delta^+/\sqrt{2} & \delta^{++} \\ \delta^0 & -\delta^+/\sqrt{2} \end{pmatrix}, \ \phi = \begin{pmatrix} \phi^+ \\ \phi \end{pmatrix} \tag{2.2}$$

After breaking electroweak symmetry as explained in the previous part for the Higgs boson we arrive with two vacuum expectation values ν and ν_Δ with $\nu \gg \nu_\Delta$. From this the ϕ^0 and δ^0 mix together into two CP-even massive states h(SM Higgs boson) and Δ^0, one CP-odd massive state χ and a Goldstone boson that is mixed into the Z boson. Furthermore, the charged states $\phi^\pm$ and $\delta^\pm$ mix into a massive charged state $H^\pm$ and a Goldstone boson $G^\pm$ that mix into the W bosons. Finally, the $\delta^{\pm\pm}$ does not mix with any other states and just gives the doubly charged Higgs $H^{\pm\pm}$. The model then generates mass to the neutrinos through a Yukawa coupling,

$$m_\nu = \sqrt{2} Y_\nu \nu_\Delta = Y_\nu \mu \nu M_\Delta \tag{2.3}$$

For decaying into leptons the decay width of the doubly charged Higgs is,

$$\Gamma_{H^{\pm\pm} \to \ell_i^\pm \ell_j^\pm} = \frac{m_{H^{\pm\pm}}}{8\pi(1+\delta_{ij})} \left| \frac{\mathcal{M}_\nu^{ij}}{\nu_\Delta} \right|^2 \tag{2.4}$$

where i, j represent the different lepton families, δ_{ij} is the Kronecker delta and $\mathcal{M}_\nu^{ij}$ is the neutrino mass matrix, defined as,

$$\mathcal{M}_\nu^{ij} = V_{PMNS}^* \, m_\nu^{diag} \, V_{PMNS}^\dagger \tag{2.5}$$

where m_ν^{diag} is a diagonal matrix with the three physical neutrino masses $m_{\nu 1}$, $m_{\nu 2}$ and $m_{\nu 3}$ along the diagonal and V_{PMNS} is the Pontecorvo-Maki-Nakagawa-Sakata(PMNS) matrix which details neutrino mixing. This thesis assumes normal mass ordering so that $m_{\nu 1} < m_{\nu 2} < m_{\nu 3}$. The doubly charged Higgs can also decay into W bosons and the relative decay branching ratio can be approximated as[20],

$$\frac{\Gamma_{H^{\pm\pm}\to\ell_i^\pm\ell_j^\pm}}{\Gamma_{H^{\pm\pm}\to W^\pm W^\pm}} \approx \left(\frac{M_\nu^{ij}}{m_{H^{\pm\pm}}}\right)^2 \left(\frac{\nu}{\nu_\Delta}\right)^4 \tag{2.6}$$

so if $M_\nu^{ij}/m_{H^{\pm\pm}} \sim 1eV/1TeV$ then the decay modes are comparable around $\nu_\Delta \approx 10^{-4}$. Each decay mode then quickly dominates with the 4th power dependence of ν_Δ as can be seen in figure 2.3. Of course the decay into W's requires a doubly charged Higgs mass above the combined mass of two W's ≈ 160 GeV.

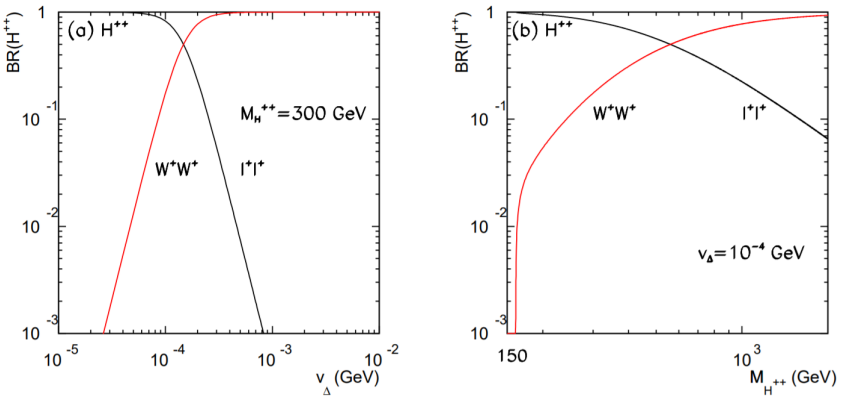

Figure 2.3: The branching ratio of the doubly charged Higgs decaying into charged leptons or W's is plotted against ν_Δ for $m_{H^{\pm\pm}} = 300$ GeV and against $m_{H^{\pm\pm}}$ for $\nu_\Delta = 10^{-4}$ GeV. For low mass and ν_Δ the lepton decay dominates and for high mass and ν_Δ the W decay dominates [20].

2.3 Lepton PDFs

The proton is a composite particle containing three valence quarks: two up quarks and one down quark. Additionally, due to quantum effects there is a constant creation and annihilation of pairs, so the proton contains a "sea" of $q\overline{q}$ quark pairs. The proton also contains gluons as the exchange boson between the quarks. A Parton Distribution Function(PDF) $f(x, Q^2)$ is a function describing the probability of finding a parton at a certain momentum fraction x within the proton. This probability also depends weakly on the momentum transfer squared Q^2. These functions are determined by performing fits to experimental deep inelastic scattering data[14].

The dependence on x and Q^2 can be seen in figure 2.4, where we see that for high x values up and down quarks dominate as most of the energy of the proton is then concentrated in the valence quarks leaving no energy for creating $q\overline{q}$ pairs. At low x the u,d quark probabilities become equal with $\overline{u}, \overline{d}$ meaning that sea quarks and gluons dominate at these values. For higher values of Q^2 there is an increase in quark-gluon interactions leading to more gluons and sea quarks[14].

Previous PDF calculations have only focused on quarks and gluons but charged leptons and photons also appear as constituents in relativistic beam particles. In [22, 23] it was shown that

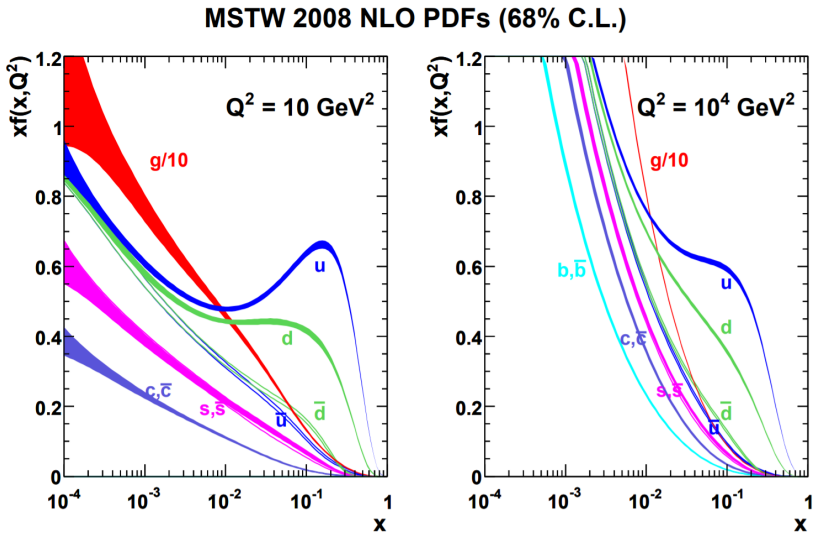

Figure 2.4: NLO PDF sets from MSTW 2008[21] for $Q^2 = 10$ GeV^2 and $Q^2 = 10^4$ GeV^2. For high x, up and down quarks dominate while for low x, sea quarks generated from gluons takes over. At high Q^2 more gluons and sea quarks are generated.

photon PDFs could be determined using electron-proton scattering. From this initial work lepton PDFs were computed in [13] leading to the **LUXlep-NNPDF31_nlo_as_0118_luxqed** PDF set. This enables searches for lepton-initiated process at hadron colliders with the possibility of having several charge and flavour combinations some which are not possible at other

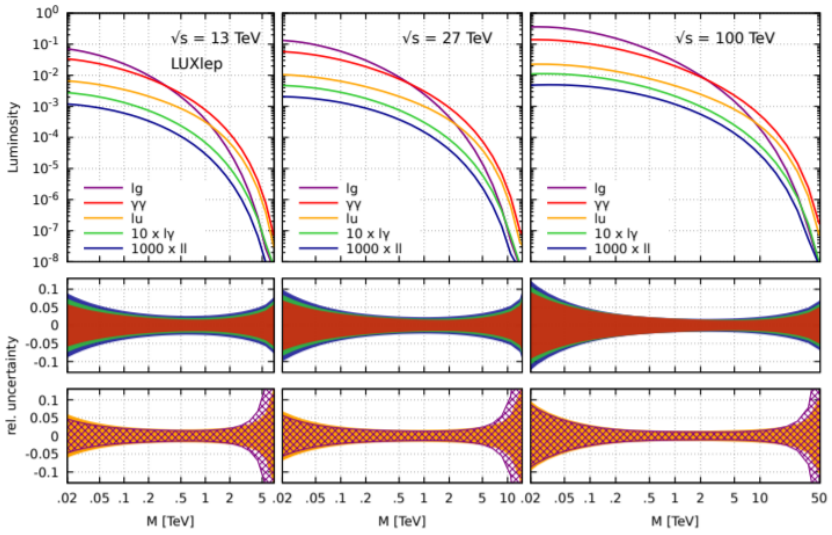

Figure 2.5: Luminosity plotted against mass of interaction for lepton-lepton, lepton-gamma, lepton-up, gamma-gamma and lepton-gluon interactions in pp-collisions at 13, 27 and 100 TeV. The values plotted here are only for electrons as the difference compared to tauons and muons is not visible in this plot. The lower part show the relative uncertainties for the different interactions with the uncertainty rising at the extreme interaction masses [13].

experiments. Luminosity values for lepton interactions in pp collisions at 13, 27 and 100 TeV are given in figure 2.5 plotted against the mass of the interaction. The interactions shown are lepton-gluon(ℓ, g), photon-photon(γ, γ), lepton-up(ℓ, u), lepton-photon(ℓ, γ) and lepton-lepton(ℓ, ℓ). The values are given for electrons as the difference to muons and tauons would not be visible. The lower panel shows the relative uncertainties for the different interactions where the uncertainty rises at the extreme interaction masses. The is a clear suppression for the lepton probability with the factor $8 \cdot 10^3$ between ℓ, ℓ and ℓ, u.

2.4 LHC

The Large Hadron Collider(LHC)[1] is the world's largest particle collider managed by the European Organization for Nuclear Research also known as CERN(Conseil européen pour la recherche nucléaire). The LHC is built in a 26.7 km circumference tunnel and is a two-ring superconducting hadron collider that can accelerate protons up to $\sqrt{s}$ =14 TeV and Pb ions up to 2.8 TeV per nucleon. The LHC has been operational for two Runs so far. Run 1 operated in 2010-2013 reaching a center of mass energy of $\sqrt{s} = 7$ TeV and $\sqrt{s} = 8$ TeV[25]. For Run 2 the energy was increased to $\sqrt{s} = 13$ TeV operating in 2015-2018[26]. In order to accelerate particles to these energies they need to be accelerated in steps as shown in figure 2.6. The LINear ACcellerator(LINAC) first accelerates the proton to 50 MeV where after it is funneled into the Proton Synchrotron Booster boosting its energy to 1.4 GeV before

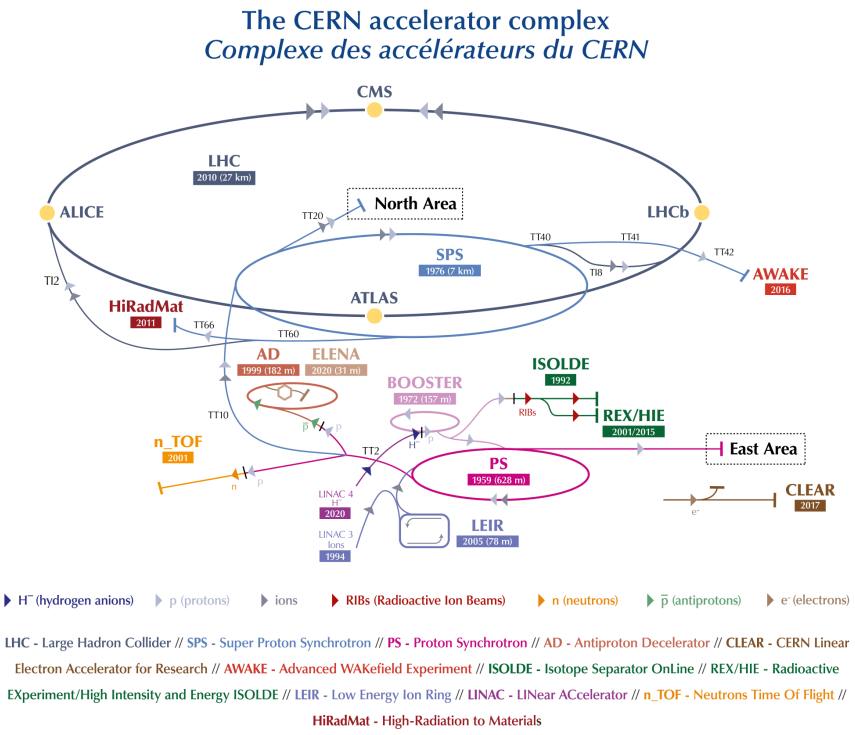

Figure 2.6: The CERN complex has many accelerators that lead up to the LHC. [24]

the protons enter the Proton Synchotron bringing the energy up to 25 GeV. Afterwards, the Super Proton Synchotron, with a circumference of 7 kilometres, accelerates the protons to 450 GeV, before entering the LHC where the protons reach the operational energy of $\sqrt{s}/2$. The two beams cross at 4 interaction points where detectors are installed to measure the resulting interactions.

One of the most important quantities at any accelerator as well as the LHC is the Luminosity L. The Luminosity is a measure of the number of collisions that happen within the beam crossings. With this value one can calculate the number of events N_{event} per second,

$$N_{event} = L\sigma_{event} \tag{2.7}$$

where σ_{event} is the cross section of the specific event. A higher luminosity is therefore the quantity to improve in order to generate more events of the specific process to study. Another important value is the integrated luminosity which is given by,

$$L_{int} = L_0\tau_L(1 - e^{-T_{run}/\tau_L}) \tag{2.8}$$

where L_0 is the initial luminosity, T_{run} the total length of the run and τ_L is the lifetime of the beam when approximated as an exponential process with the losses mainly coming from beam collisions and emittance blow-up due to scattering with residual gas and intrabeam[1].

A Toroidal LHC ApparatuS(ATLAS) and Compact Muon Solenoid(CMS) are both general-purpose detectors operating at a peak luminosity of $L = 10^{34}$ cm^{-2}s^{-1}. LHC beauty(LHCb) focuses on physics related to beauty quarks at a lower luminosity of $L = 10^{32}$ cm^{-2}s^{-1}. A Large Ion Collider Experiment(ALICE) is a ion experiment using colliding Pb ions at a luminosity of $L = 10^{27}$ cm^{-2}s^{-1} to simulate quark gluon plasma, a state of matter where quarks and gluons are free [1].

2.5 ATLAS

The ATLAS detector[2] is the world's largest general-purpose detector, 46 m long and 25 m in diameter, weighing 7000 tonnes. The general purpose design enables a wide range of physics searches such as the discovery of the Higgs boson, supersymmetry models, properties of the top quark, CP violation and dark matter. The detector is built with the aim to ensure that the decay products of all these physics processes can be measured precisely. To do this a layered design is implemented with four distinct layers: Magnet System, Inner Detector(ID), Calorimetry and Muon Spectrometer.

The magnet system consists of one solenoid surrounding the inner-detector and three toroids around the calorimetry. The ID implements tracking systems in order to measure the momentum of the particles passing through. The calorimetry can be divided into two parts, Electromagnetic and Hadronic, which specialized in measuring the energy of different type

of particles. Outside of the calorimeters is the muon spectrometer which measures muon momentum using layering of tracking chambers.

The coordinate system of ATLAS is defined with the origin at the nominal interaction point, with the beam direction defining the z-axis and the x-y plane transverse to the beam direction. The positive x-direction is inwards to the center of the LHC ring and the positive y-direction is upwards. The azimuthal angle ϕ is measured around the z-axis going from $-\pi$ to π and the polar angle θ is the angle from the z-axis. The pseudorapidity, defined as,

$$\eta = -\ln\left(\tan\left(\theta/2\right)\right) \tag{2.9}$$

is used instead of the θ angle(for massive object the rapidity y=$1/2\ln\left[(E+p_z)/(E-p_z)\right]$ is used instead). Pseudorapidity is used because particle production is approximately constant as a function of rapidity and differences in rapidity are Lorentz invariant along the beam axis. The variables η and ϕ can be combined into an angular distance in pseudorapidity-azimuthal angle space defined by,

$$\Delta R = \sqrt{(\Delta\eta)^2 + (\Delta\phi)^2} \tag{2.10}$$

Certain transverse variables, for example p_T, E_T and E_T^{miss}, are also used as they are invariant to boosts along the beam-axis and are defined by,

$$p_T = \sqrt{(p_x^2 + p_y^2)} \tag{2.11}$$

and similarly for the other variables.

2.5.1 Magnet System

The ATLAS magnet system consists of four superconducting magnets. The magnetic system is 22 m in diameter and 26 m in length and is capable of storing 1.6 GJ of energy. The system shown in figure 2.7 consists of one solenoid, one barrel toroid and two end-cap toroids. The solenoid is located within the calorimeter volume and is aligned to the beam axis. This provides a 2 T magnetic field along the beam axis within the inner detector. The barrel toroid and its magnetic field surrounds the calorimetry and the end-cap toroids. The end-cap toroids are located one both sides of the detector providing a magnetic field for particles with high pseudorapidity.

2.5.2 Inner Detector

The first part of the detector after the interaction is the Inner Detector(ID). The ID is designed to perform accurate pattern recognition, momentum resolution and primary and secondary vertex measurement for charged tracks with a p_T threshold of 0.5 GeV and pseudorapidity range of $|\eta| < 2.5$. Additionally, it can also identify electrons with $|\eta| < 2.0$ and energies between 0.5 GeV $-$ 150 GeV. The detector needs to handle the 1000 particles that

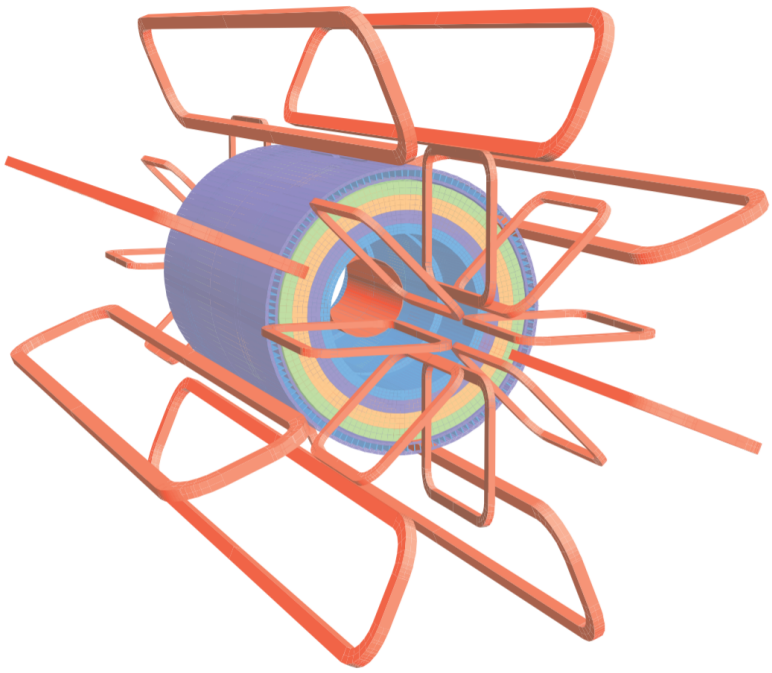

Figure 2.7: Geometry of the magnet system at the ATLAS detector. Eight barrel toroids can be seen with end-cap toroid on each side. The solenoid is located in the middle inside the calorimeter volume[2].

travel from the interaction point to the detector every 25 ns. The inner detector consists of three sub-detector types with the layout illustrated in figure 2.8. From inner to outer the sub-detectors are semiconductor pixel detector, silicon microstrip(SCT) trackers and transition radiation tracker(TRT). The pixel and SCT are arranged in concentric circles in the barrel region while for the endcap, the pixel and SCT are arranged in circles perpendicular to the beam axis. The TRT is arranged in parallel around the barrel region and radially out from the beam axis in the endcap.

The Pixel detector is designed to perform high accuracy measurements while withstanding an intense high-radiation environment. The layers are segmented in R$-\phi$ and z with each track commonly crossing three layers. All of the sensors are identical and have a minimum pixel size of R$-\phi$ $\times$ z of 50 $\times$ 400 μm^2. The accuracy of the detector is 10 μm(R-ϕ) and 115 μm(z) in the barrel and 10 μm(R-ϕ) and 115 μm(R) in the end-caps. In total the pixel detector has 80.4 million readout channels.

The SCT consists of 4088 modules of silicon strip detectors with 2112 modules located on the four concentric barrels and 988 modules in total on 9 disk for the two endcaps. Typically a track crosses eight strip layers which gives four space points. The accuracies per module are 17 μm(R-ϕ) and 580 μm(z) in the barrel region and 17 μm(R-ϕ) and 580 μm(R) for the disks. The total number of readout channels is approximately 6.3 million.

The TRT comprises of 4 mm drift straw tubes, generating tracking up to $|\eta| < 2.0$. The tubes are 144 cm and perpendicular to the beam line in the barrel region. For the endcap

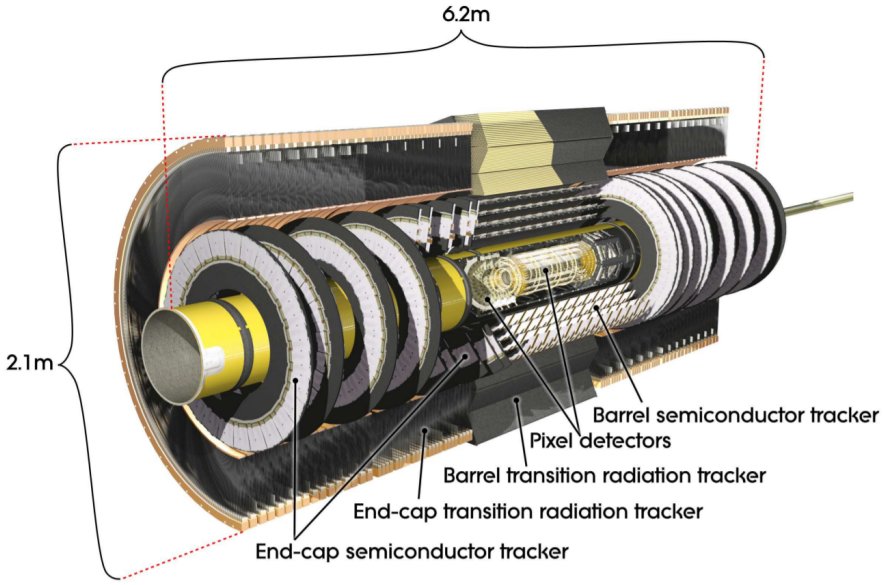

Figure 2.8: The inner detector of the ATLAS detector consisting of the pixel, SCT and TRT. Within the barrel the pixel and SRT are arranged in concentric circle while the TRT is arranged parallel to the beam axis. Within the end-cap the pixel and SCT are arranged on circles perpendicular to the beam axis while the TRT is arranged radially from the beam axis[2].

the tubes are 37 cm and arranged radially like wheels. The TRT typically registers 36 hits per track but only performs measurements in R-ϕ with an accuracy of 130 μm. In total the TRT has approximately 351,000 readout channels.

2.5.3 Calorimetry

The calorimetry of the ATLAS detector consists of different parts covering a range of $|\eta| < 4.9$ with different requirements for physics purpose and radiation environments dictating the design. For the same range as the inner detector $|\eta| < 2.5$ the EM calorimeter is primarily designed to precisely measure electrons and photons, while the remaining coarser calorimetry is sufficient enough for jet reconstruction and E_T^{miss} measurements. The calorimeter depth is the result of a compromise between maximizing muon punch-through into the muon spectrometer and adequate containment for electromagnetic and hadronic showers. The number of interaction lengths before the muon system mainly varies between 10-14 with the calorimetry contributing around 9-11 interaction lengths to the total.

The electromagnetic calorimeter consists of the barrel part for $|\eta| < 1.475$ and two endcaps for $1.375 < |\eta| < 3.2$. The calorimeters are lead-liquid argon detector with accordion shaped electrodes and lead absorbers. The geometry enables several active layers, three layers for $|\eta| < 2.5$ and two layers for $2.5 < |\eta| < 3.2$ as well as the overlap between the electromagnetic endcap and barrel region. The forward calorimeter provides electromagnetic cover at $3.1 < |\eta| < 4.9$. In the region $|\eta| < 1.8$, the Electromagnetic calorimeter is complemented by a

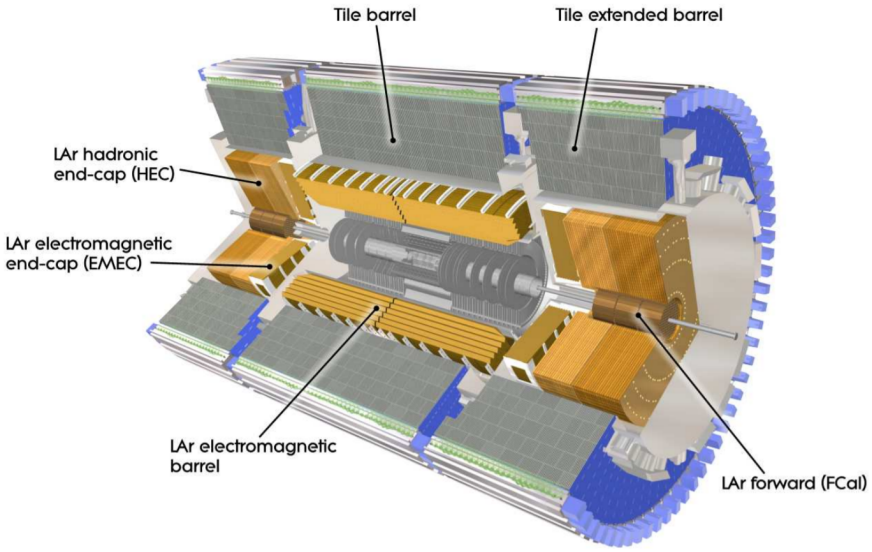

Figure 2.9: The calorimetry of the ATLAS detector consisting of the lAr electromagnetic barrel, lAr electromagnetic end-cap, Tile hadronic barrels, lAr hadronic end-cap and lAr forward calorimeters. They all combine to cover a range of $|\eta| < 4.9$ optimised for electron, photons and jets while enabling optimal muon punch-through [2].

presample detector that attempts to correct for the energy loss by electrons and photons upstream.

The hadronic calorimetry consists of two parts, the tile calorimeter and the hadronic end-cap calorimeter. The tile calorimeter is placed directly outside the electromagnetic calorimeter as seen in figure 2.9 with its barrel covering $|\eta| < 1$ and two barrels that extend outside the end-caps that covers $0.8 < |\eta| < 1.7$. The tile calorimeter is a sampling calorimeter with scintillating tiles as the active material and steel as the absorber. The hadronic end-cap calorimeter consists of two independent wheels per end-cap and are located behind the electromagnetic end-cap. The calorimeter is a sampling calorimeter with lAr as the active material and copper absorbers. The initial part of the end-cap extends further towards the beam giving the calorimeter the coverage of $1.5 < |\eta| < 3.2$.

Finally, the forward calorimeter is located close to the beam within the hadronic end-cap calorimeter. To minimize neutron albedo within the inner detector cavity the forward calorimeter starts about 1.2 m past the front face of the EM calorimeter. Due to this, the length of the forward calorimeter is limited which forces a high-density design where the lAr active regions are very thin. The calorimeter is divided into three parts, the first part uses copper as the absorber and is optimized for electromagnetic measurements, while the last two use tungsten instead and are focused on hadronic measurements.

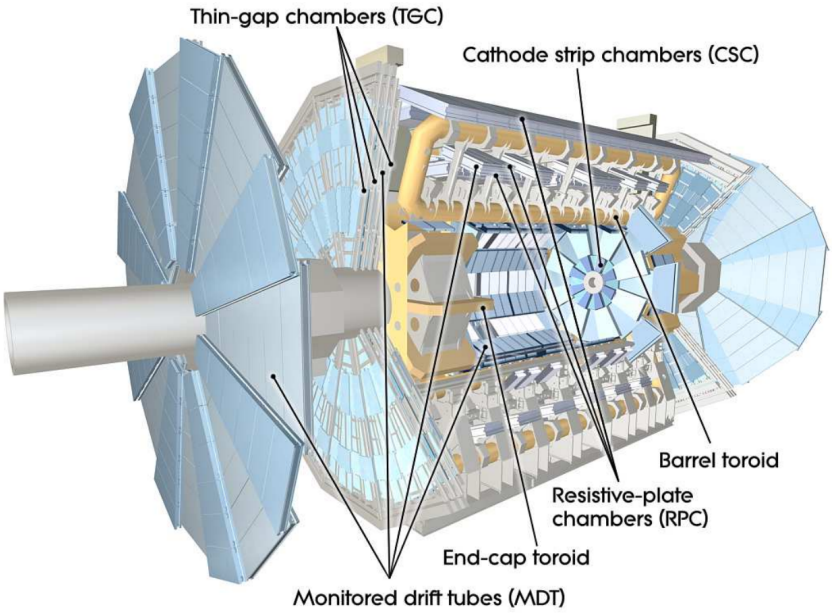

Figure 2.10: The muon system of the ATLAS detector shown in a cut-away view with the inner detector and the calorimetry removed. The four different parts of the system are marked, MDT and CSC are used for precision tracking while RPC and TGC are used for triggering[2].

2.5.4 Muon Spectrometer

The muon spectrometer is illustrated in figure 2.10, and uses the deflection of the muon tracks by the magnet system as the basis for its p_T measurements. The muon spectrometer consists of four subsystems located in three layers(cylindrical around beam axis in the barrel and perpendicular to the beam axis in the end-cap): Monitored Drift Tubes(MDT) and Cathode Strip Chambers(CSC) for precision tracking and Resistive Plate Chambers(RPC) and Thin Gap Chambers(TGC) for triggering. For $|\eta| < 1.4$, the magnetic bending is provided by the superconducting toroid barrel magnets, while the end-cap toroid magnets cover $1.6 < |\eta| < 2.7$, with a combination of the two in the region between. The MDT covers $|\eta| < 2.7$ while the CSC are used in $2.0 < |\eta| < 2.7$, designed to withstand the larger rate and background conditions by having a higher granularity. For triggering, the RPC covers $|\eta| < 1.05$ in the barrel while the TGC covers $1.05 < |\eta| < 2.4$ in the end-cap.

2.5.5 Triggering

The interaction event rate at the LHC occurs with approximately 1 GHz at the design luminosity of 10^{34} cm^{-2}s^{-1}, which for run 2 has been increased. The data recording is limited to approximately 1.2 kHz due to resource and technology constraints. The trigger system of ATLAS[27] is responsible for this rejection factor of 8.3×10^5, with the main purpose of maximizing the sensitivity to new physics. The trigger system is divided into three parts: Level-1(L1) trigger, Level-2(L2) trigger and the event filter, where the L2 and event filter are usually combined together and called the High-Level Trigger(HLT). The trigger levels refine

the decision using increasing accuracy with additional and more stringent criteria.

The L1 trigger uses a subset of the detector information to reduce the rate to around 100 kHz within 2.5 μs. The triggering is done using custom-made electronics and searches for signals from muons, jets, electrons, photons, tau-leptons decaying hadronically and also passes events with large missing transverse energy E_T^{miss}. The L1 trigger also identifies Regions of Interest(RoI) in η and ϕ, where the selection procedure has found features passing the threshold. These RoI's are then sent to the L2 trigger which uses all the accessible detector information within them. With this the L2 reduces the event rate further with an average event processing time of 40 ms. Finally, the event filter performs full-event offline analysis to further reduce the rate to the final value of around 1.2 kHz with an average event processing time of 4 s. The HLT triggers use the full granularity and accuracy of the detector using data from the calorimetry, muon spectrometer and inner detector tracker.

Chapter 3

Simulation

In this chapter the details regarding simulation of the data will be given first. Truth level information, simulation values before simulation of the detector is performed, will be discussed and finally the derivation used in this thesis is explained.

3.1 Pythia8

The initial idea was to use MadGraph5_aMC@NLO[28]+Pythia8[29] to simulate the signal process. As Pythia8 is not able to handle lepton PDFs so far the attempt focused on moving back in the Feynman diagram of the process to $\gamma + \gamma \to H^{\pm\pm} + \ell^{\mp} + \ell^{\mp}$ as Pythia does handle photon PDFs. An attempt was made to simulate this process but due to the doubly charged Higgs direct coupling to the photon, this process generated Feynman diagrams that did not contribute to the lepton initiated process this thesis aims to study. Therefore, it was decided to move to Herwig[30, 31] for parton showering.

3.2 Signal

The signal sample was generated at Leading Order(LO) at $\sqrt{s} = 13$ TeV using MadGraph5_aMC@NLO v3.3.1[28], Herwig v7.2.2[30, 31] and EvtGen[32]. 16000 events were generated in two separate batches of 8000 events for each mass point of $m_{H^{\pm\pm}} = 10, 50, 100, 250$ GeV. The sample was generated with the type-II seesaw model under normal neutrino mass ordering defined in [7] with default model parameters listed in table 3.1. The parton distribution function used was the **LUXlep-NNPDF31_nlo_as_0118_luxqed** [13] set described in section 2.3. For the parton shower, the shower tune were set to the Herwig defaults.

The file generated after hard event scattering and parton showering was then worked through the ATLAS simulation and reconstruction using the MC16 campaign(Monte Carlo settings corresponding to the latest data taking year of 2018) to simulate the interaction with the detector. The simulation was done with Geant4[33] using ATLFastII[34] which simulates the calorimeter with FastCaloSim[35] which leads to faster simulation, the rest of the calorimeter is simulated in Geant4 as usual. ATLFastII performs well compared to full detector

simulations with few differences observed for leptons. Simulation of pile-up events, multiple proton-proton interactions in the bunch crossings, were generated using Pythia8 with minbias tunes.

Table 3.1: Table details the default model parameters used in the MadGraph5_aMC@NLO generation.

Model Parameter	Value
λ_{HD1}	1.0
λ_{D1}	1.0
ν_D	10^{-10} GeV
$m_{\nu 1}$	$5 \cdot 10^{-2}$ eV
m_h	125 GeV
m_{Δ^0}	500 GeV
$m_{H^\pm}$	503 GeV
$m_{H^{\pm\pm}}$	[10,50,100,250] GeV

Due to a bug that could not be resolved during this project, events with muons as the initial particle could not be simulated. The problem that occurred was that the doubly charged Higgs created by the muons would have a z coordinate at around $\approx 10^{23}$ mm. The next doubly charged Higgs in the event list would then go back to a more "normal" position with a z position closer to the origin around 10^{-9} mm. Due to this problem, only events with electrons producing the doubly charged Higgs were used as signal samples in this thesis. Overall, $e^\pm e^\pm$, $\mu^\pm \mu^\pm$ and $\tau^\pm \tau^\pm$ initiated processes dominate over mixed-flavour ones and the p_T distribution for these three processes are shown in figure 3.1. The p_T distribution for the electron induced events used in this thesis is not very different from the p_T in muon production, while tauon production yields a boost. This boost would give the decay leptons a larger p_T and with the boost the ϕ angle between the leptons would be less narrow around π than what is simulated in this thesis.

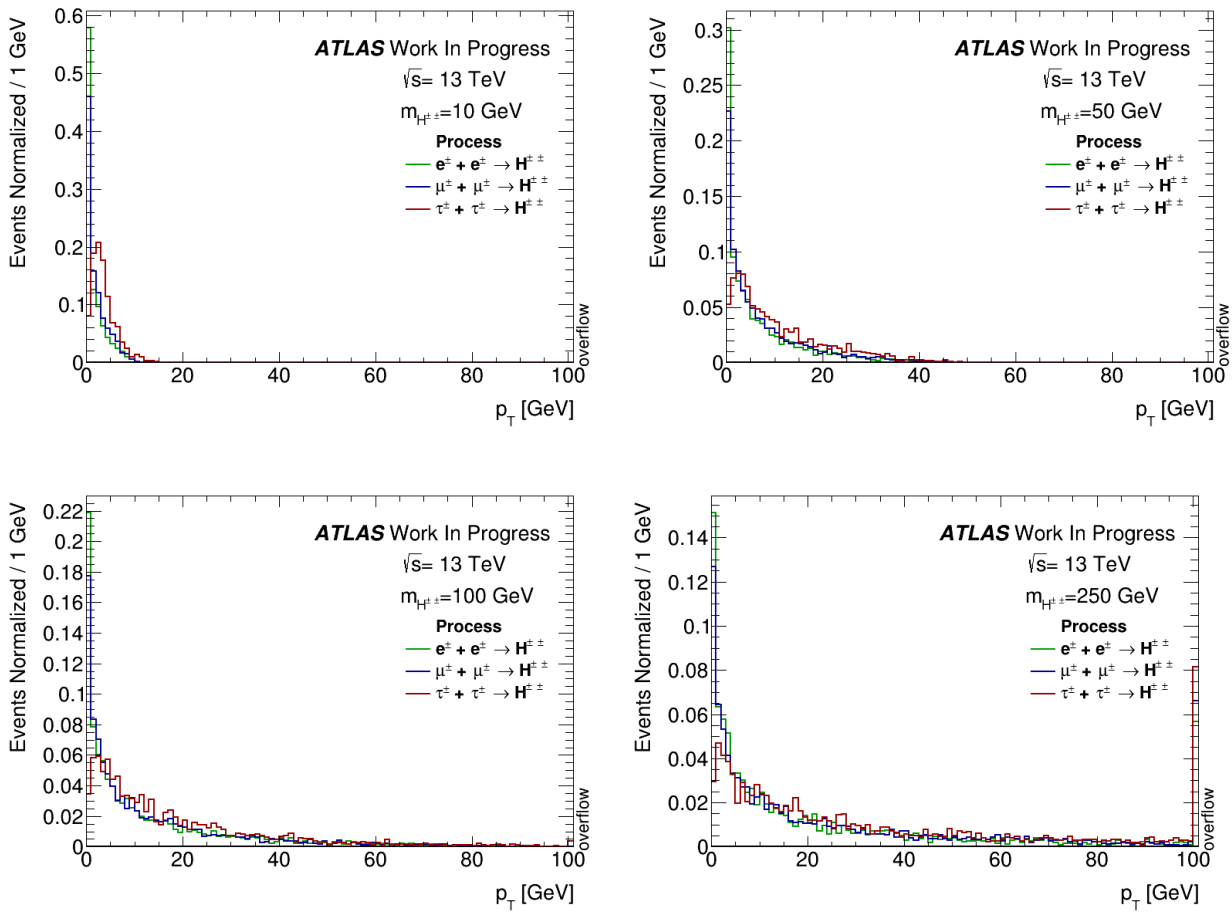

Figure 3.1: The p_T of the doubly charged Higgs plotted normalized to 1 for the three main production processes and for the four different mass points. Between muons and electrons there is not that large difference between the doubly charged Higgs p_T for all mass points. In the tau produced case the p_T is definitely boosted a bit compared to the electron and muon cases.

3.3 Simulation Truth

In this section truth values of the data are plotted for the different mass points. Truth is the simulated data before simulation and reconstruction of the ATLAS detector is performed. Figure 3.2a shows the p_T distribution of the doubly charged Higgs at its different mass points. The overall p_T of the doubly charged Higgs is quite low meaning that the decay will be an opposite side decay in the x-y plane. This property of the decay could be used to eliminate background in reconstruction. Lower mass of the doubly charged Higgs has a lower p_T distribution.

Figure 3.2b shows the η distribution for the different mass points. Lower mass has a wider distribution, while for higher mass there is a more narrow distribution, due to the higher p_T. Important factor to remember is the η coverage of the inner detector at ATLAS being

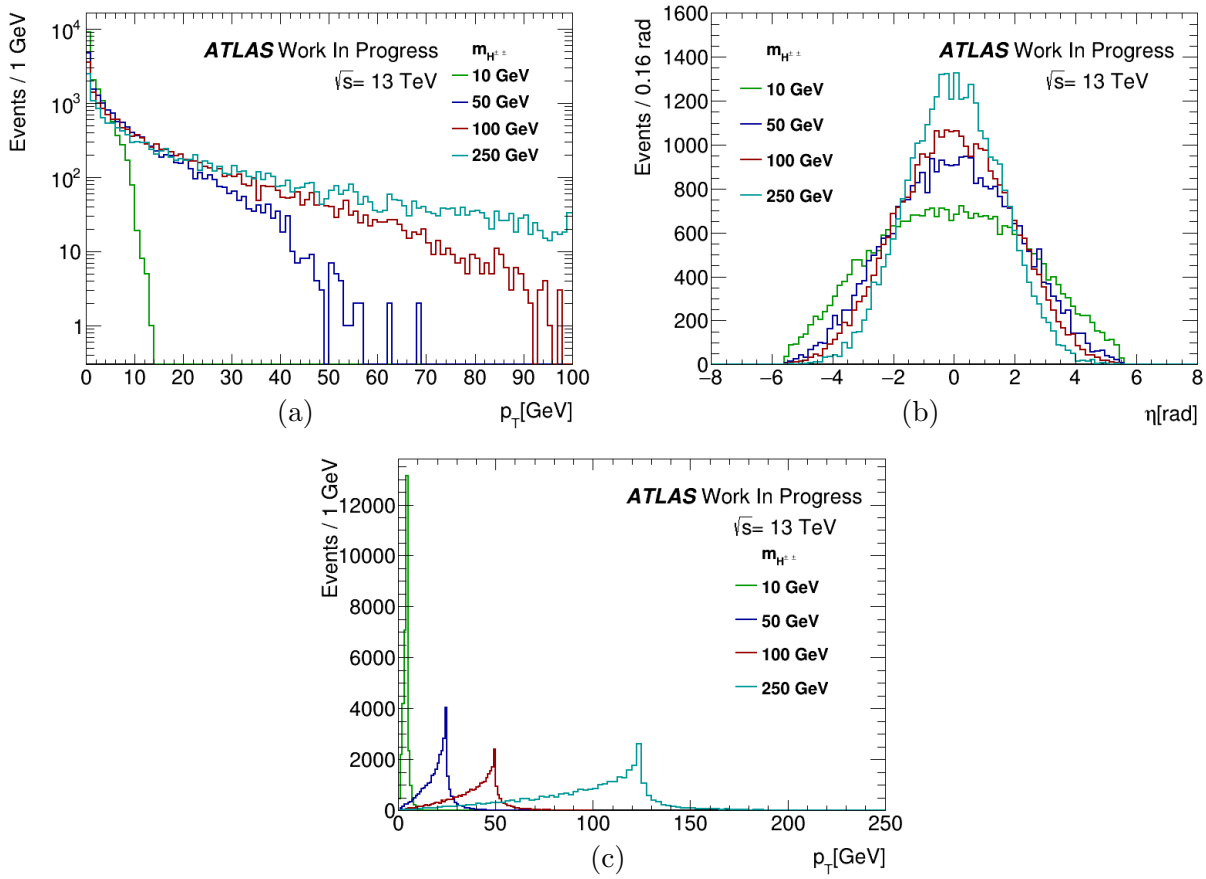

Figure 3.2: (a) The p_T distribution at truth level for the doubly charged Higgs at the different mass points. Distribution is quite low in pT with the lower mass points having lower distributions. (b) The η at truth level is plotted for the different mass points. Lower mass has a wider distribution and higher mass a more narrow distribution. (c) The p_T distribution at truth level for the daughters of the doubly charged Higgs at the different mass points. Peak of the distribution is located at $m_{H^{\pm\pm}}/2$.

$|\eta| < 2.5$ so leptons outside this cut-off will not be reconstructed. This means that the lower mass points loose more leptons just due to its wider η distribution.

Figure 3.2c shows the p_T distribution for the different mass points of the doubly charged Higgs. The peak of the distribution is clearly located at $m_{H^{\pm\pm}}/2$. The fall off after the peak is quite steep with the lower p_T side having a longer tail. This is due to the non-boosted nature of the decay with the p_T of the doubly charged Higgs being quite low as seen in figure 3.2a.

The decay process distribution of the doubly charged Higgs is shown in figure 3.3. The category of *else* indicates that something other than the expected decays occurred. Same-lepton decay is preferred with muons and tauons having a slightly higher probability compared to electrons. There is a model dependence on these decay distributions with a high dependence on the neutrino masses. The cause of the increase in *else* processes at 10 GeV is unclear. These events are mainly events where the doubly charged Higgs only decays into one lepton

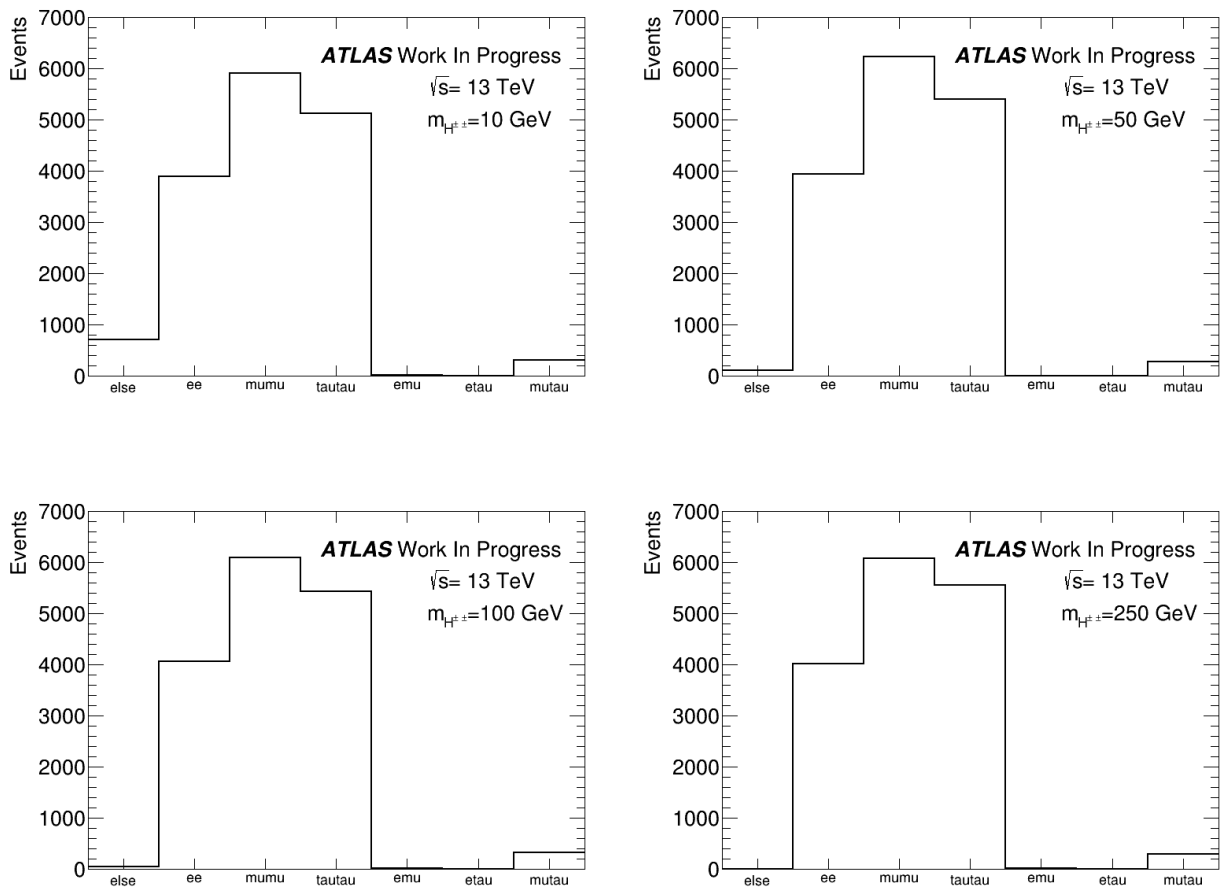

Figure 3.3: The decay processes of the doubly charged Higgs is plotted for all lepton combinations and with an else option if none of the other combinations apply. Distribution is similar for all masses with same-flavour charged lepton decay dominating. The 10 GeV mass point have an increase in the other type of decays. For all datasets the total events add up to 16000.

and sometimes photons which should not be an allowed decay and indicates some problem in the simulation. This is not a problem in the Herwig output so it might be due to some p_T cut within the ATLAS simulation, the difference across mass points also might indicate a p_T problem. These events will be counted to the total events but will not be able to be reconstructed in this analysis. Other than these outliers the decay processes are very similar across mass points.

3.4 Derivation

A derivation of the simulated data sample was used for the final analysis. The main purpose of this was to add truth connections to the dataset in order to match reconstructed particles to its truth counterpart but the derivation also adds other variables. In this analysis the

EXOT0 derivation was used, which is optimized for dilepton searches. Derivations implement thinning and slimming which is the removal of data containers and variables within them that will not be needed. Further, skimming(event selection) of the data required two electrons or muons with $p_T > 20$GeV and at least *Loose* quality which all events passed.

Chapter 4

Event Reconstruction

In order to perform an accurate analysis the signal needs to be reconstructed and identified. Different selection cuts can be optimised for the greatest signal strength that reduces background particles coming from processes such as mainly pile-up and other background particles within the event. For this analysis same-flavour pairs of electrons, muons and hadronically decaying taus are the signal particles. In this section the cuts used in this thesis will be motivated and described.

4.1 Reconstruction cuts

The reconstruction cuts within this section will be based on *LHMedium* electrons and muons. The *LHMedium* and *LHTight* identification working points are based on detector information and analyzed with a multivariate likelihood discriminant detailed in Ref. [36] for electrons and Ref. [37] for muons. The cuts will be determined for medium and tight selections which should correspond to an upper and lower limit on the number of events, with a potential for higher background rejection with tight selections.

4.1.1 p_T cuts

The p_T distribution of medium working point electrons and muons for events with at least 2 medium electrons or muons are plotted in figure 4.1 and 4.2. Two histograms are plotted with signal and background leptons for the four different mass points. For electrons there is a large overlap between background and signal at lower mass points, at higher masses there are still many background electrons but the overlap is not as large. A p_T cut have been implemented to remove background electrons at the higher mass points for two different levels of selection: medium and tight. These selections can be seen in table 4.1.

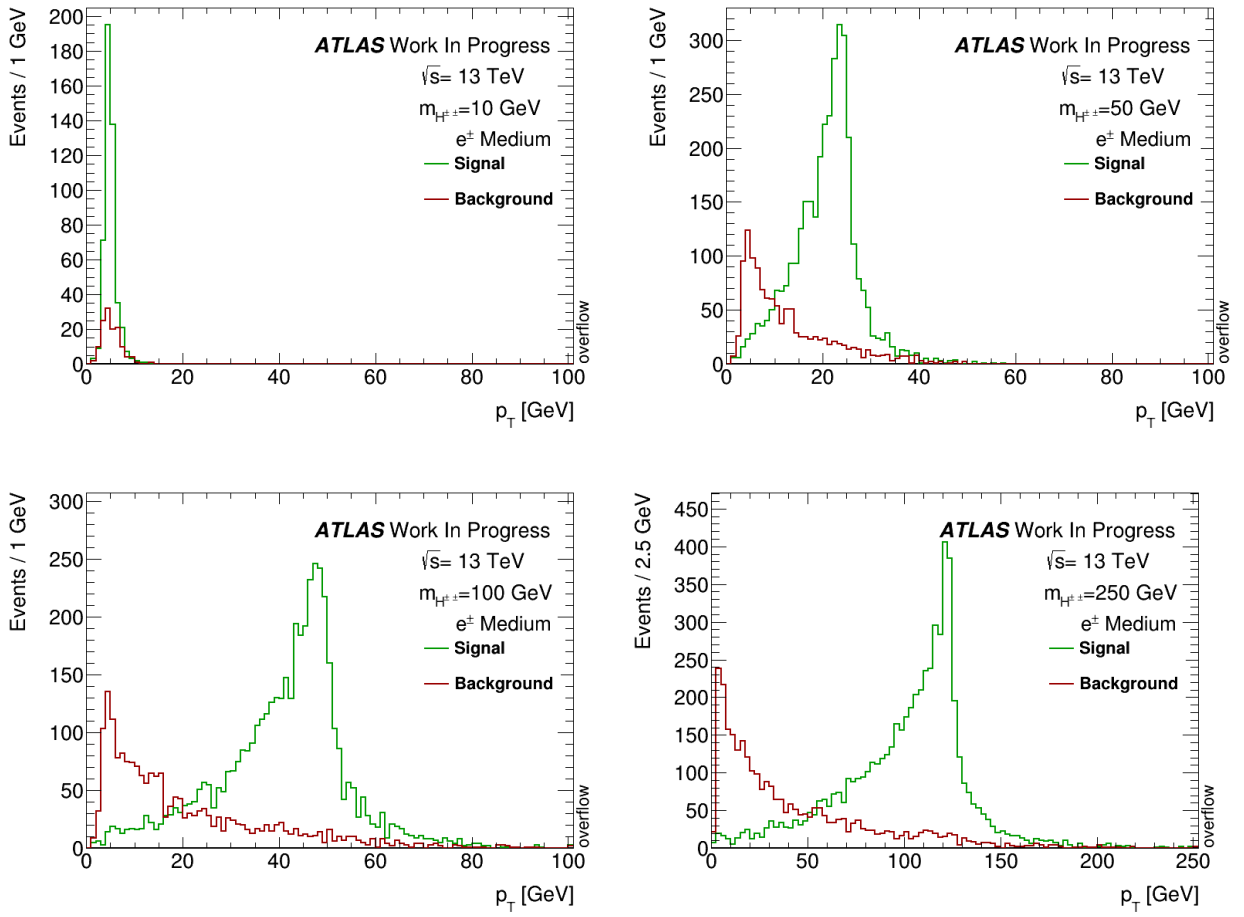

Figure 4.1: The p_T distribution is plotted with medium working point electrons for the four different mass points. Only electrons from events with more than 2 medium electron are added in histograms for both signal and background electrons. The overlap between background and signal electron is vastly different between the mass points.

Table 4.1: p_T cuts for medium and tight electrons used within this thesis.

Electron Type	$m_{H^{\pm\pm}} = 10$ GeV	$m_{H^{\pm\pm}} = 50$ GeV	$m_{H^{\pm\pm}} = 100$ GeV	$m_{H^{\pm\pm}} = 250$ GeV
Medium	$p_T > 0$ GeV	$p_T > 5$ GeV	$p_T > 10$ GeV	$p_T > 20$ GeV
Tight	$p_T > 0$ GeV	$p_T > 10$ GeV	$p_T > 15$ GeV	$p_T > 35$ GeV

For muons in figure 4.2 there is a larger overlap between background and signal at lower mass points. Overall the amount of background muons is quite low and at higher mass points there is a clear seperation between signal and background in p_T. A p_T cut have been implemented to remove background muons at the higher mass points for two different levels of selection: medium and tight. The selections used within this thesis for muons can be seen in table 4.2.

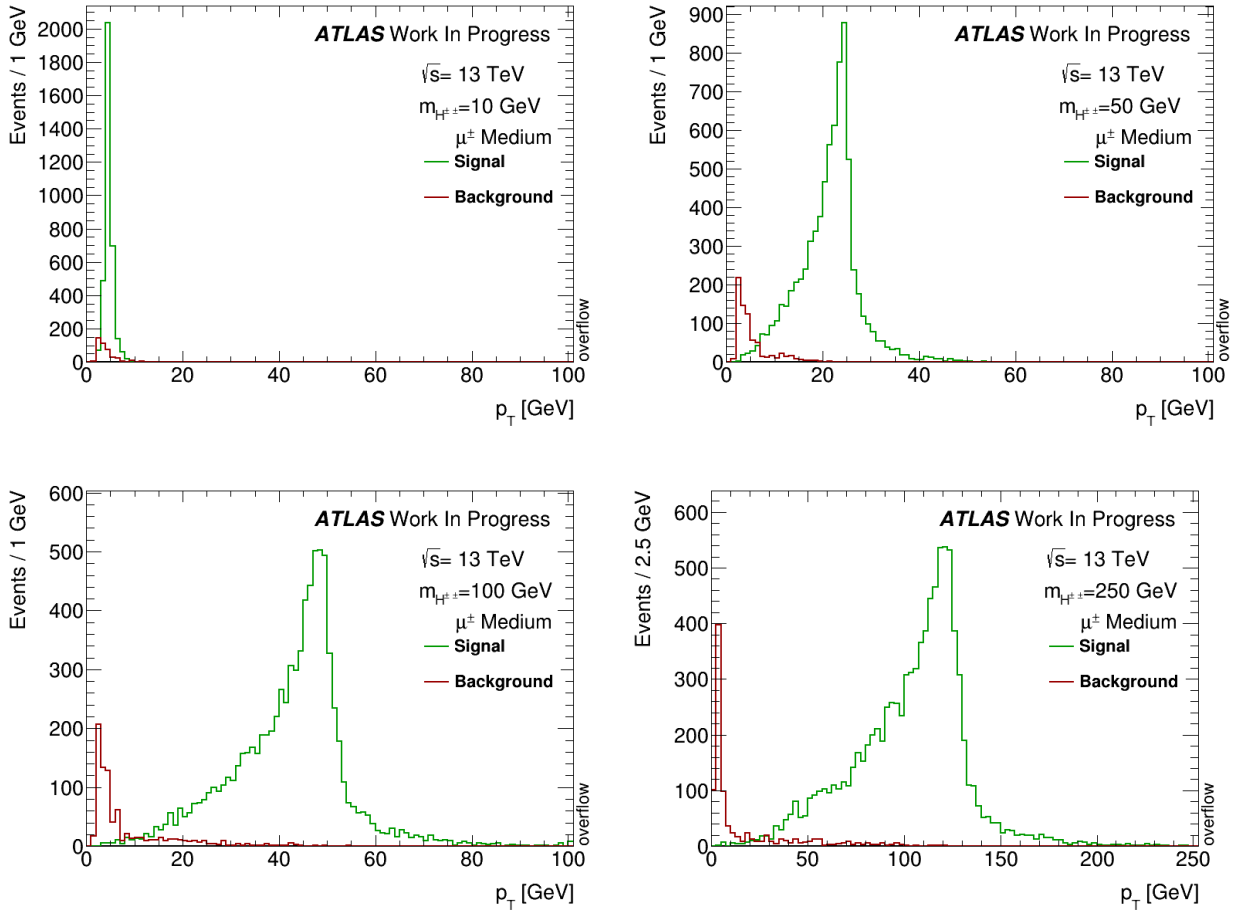

Figure 4.2: The p_T distribution is plotted with medium working point muons for the four different mass points. Only muons from events with more than 2 medium muon are added in histograms for both signal and background muons. The overlap between background and signal muon is vastly different between the mass points.

Table 4.2: p_T cuts for medium and tight muons used within this thesis.

Muon Type	$m_{H^{\pm\pm}} = 10$ GeV	$m_{H^{\pm\pm}} = 50$ GeV	$m_{H^{\pm\pm}} = 100$ GeV	$m_{H^{\pm\pm}} = 250$ GeV
Medium	$p_T > 0$ GeV	$p_T > 5$ GeV	$p_T > 7.5$ GeV	$p_T > 10$ GeV
Tight	$p_T > 0$ GeV	$p_T > 10$ GeV	$p_T > 12.5$ GeV	$p_T > 30$ GeV

4.1.2 d_0 cut

The impact parameter d_0 is defined as the closest distance between the track and the beam axis in the transverse plane. In order to remove background from pile-up and other sources, a cut on d_0/σ_{d_0} is generally recommended to be 3.0 for muons and 5.0 for electrons within ATLAS. Figure 4.3 shows the distribution of d_0/σ_{d_0} for medium electrons within events that have at least two medium electrons. A cut at 5.0 would not eliminate any substantial amount

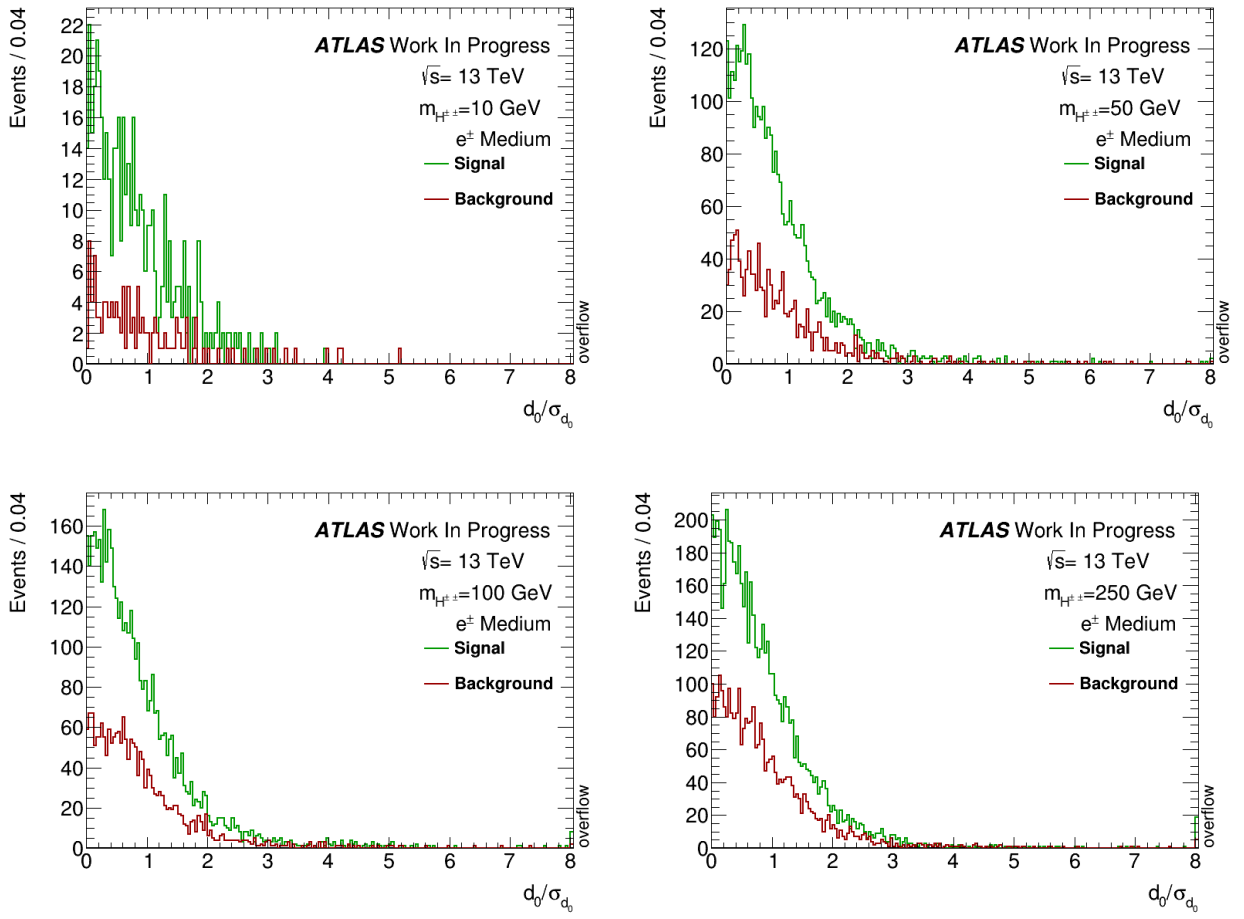

Figure 4.3: The d_0/σ_{d_0} distribution is plotted with medium working point electrons for the four different mass points. Histograms for both signal and background electrons are plotted. There is not a good cut to remove background electrons that would not also remove signal electrons.

of background electrons at any mass point. For a looser selection no cut will be made and for a tighter selection the recommended cut of 5.0 will be used.

The distribution for medium muons is shown in figure 4.4 for events that have at least two medium muons. Here, a cut could be used to eliminate some background with not that many signal muons being removed as well. At 10 GeV there is a substantial amount of signal muons above a cut of 3. The decision was made to implement no cut in the looser selection and for the tighter selection the recommended cut of 3.0 is used.

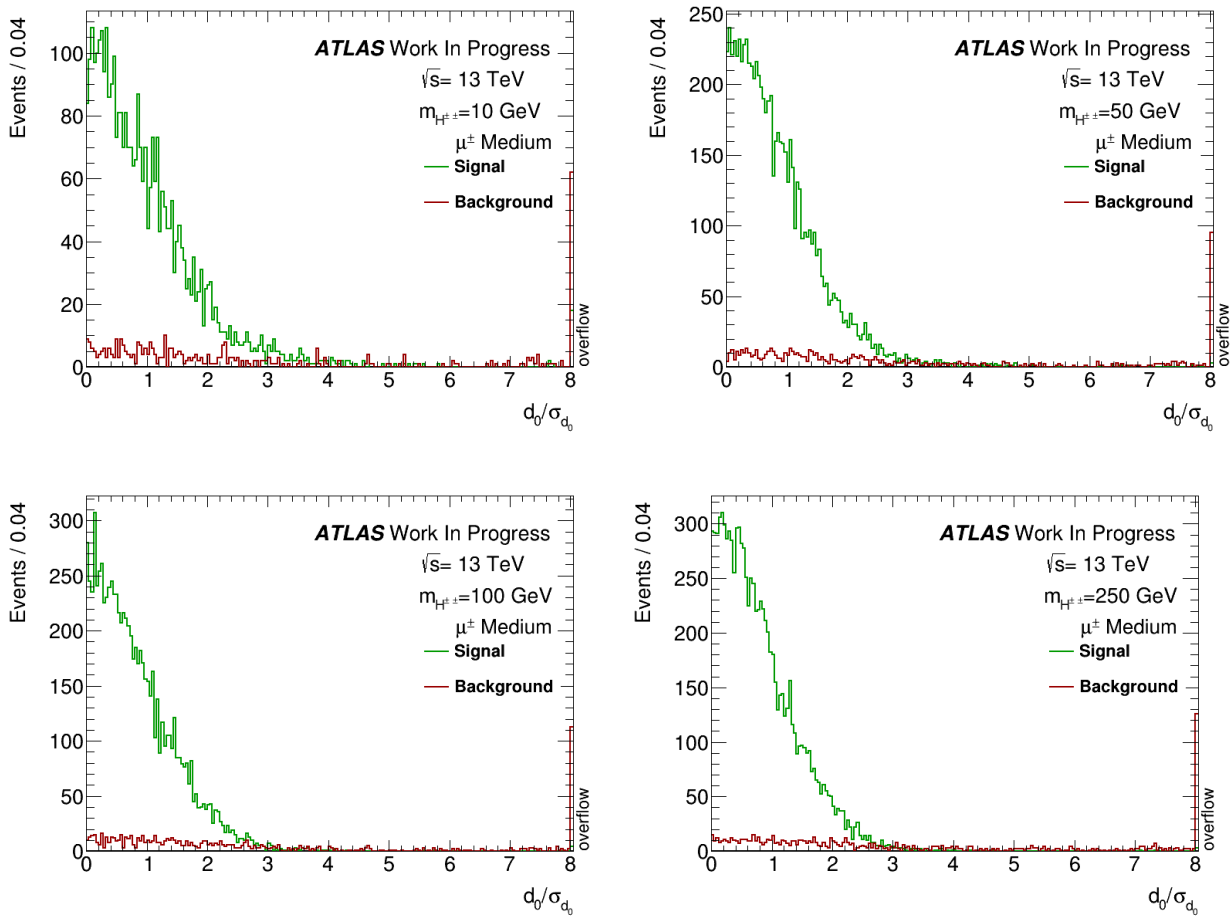

Figure 4.4: The d_0/σ_{d_0} distribution is plotted with medium working point muons for the four different mass points. Histograms for both signal and background muons are plotted. There is a large overflow especially for the background muons.

4.1.3 $\Delta z_0 sin(\theta)$ cut

The longitudinal impact parameter Δz_0 is defined as the distance between the track and the primary vertex of the event in the z direction. The primary vertex is defined as the vertex with the largest $\sum p_T^2$. This value is commonly multiplied with the sine of the angle to the z axis, θ, to mitigate rejection of tracks in the forward region due to their higher uncertainties. The recommended cut for both electrons and muons is 0.5 mm. In figure 4.5 the $\Delta z_0 sin(\theta)$ distribution is shown for medium electrons in events with at least two medium electrons. There is no apparent cut that would eliminate a substantial amount of background electrons without also eliminating signal electrons at all mass points. For electrons within the 10 GeV data set there is a large number of overflow with $\Delta z_0 sin(\theta)$ values over 10 mm. A final cut of 0.5 mm was used for the tight selection of electrons and no cut was used for the medium selection.

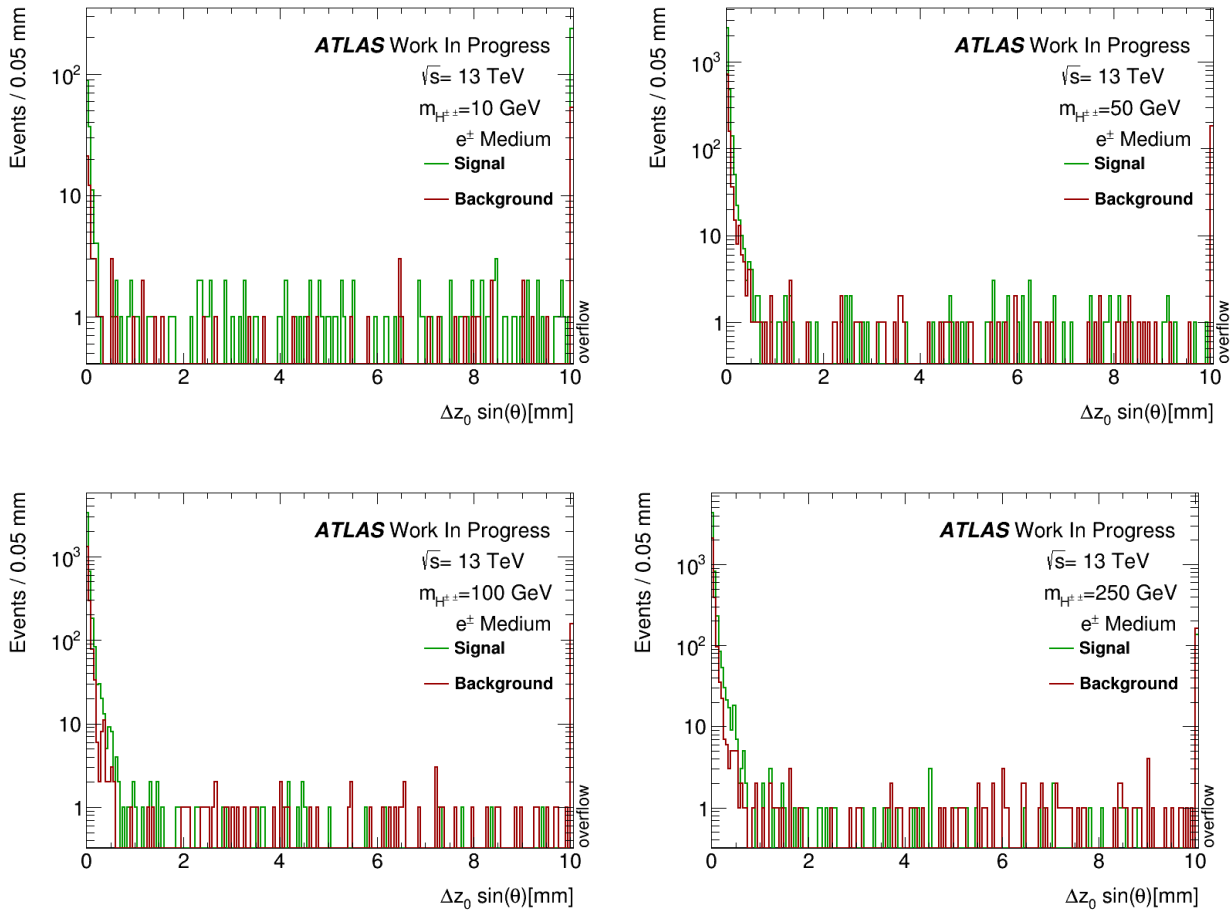

Figure 4.5: The $\Delta z_0 sin(\theta)$ distribution is plotted with medium working point electrons for the four different mass points. Histograms for both signal and background electrons are plotted. There is a large overflow on all plots and for $m_{H^{\pm\pm}} = 50, 100$ GeV the overflow bin overlaps between signal and background.

In figure 4.6 the $\Delta z_0 sin(\theta)$ distribution is shown for medium muons in events with at least two medium muons. For the 10 GeV data set the values are very large with a substantial overflow over 10 mm. For the other datasets there is a possibility to use a cut at 0.5 mm to reduce background muons. Some signal muons would also be excluded with this cut. A final cut of 0.5 mm was used for the tight selection and no cut was implemented for the medium selection.

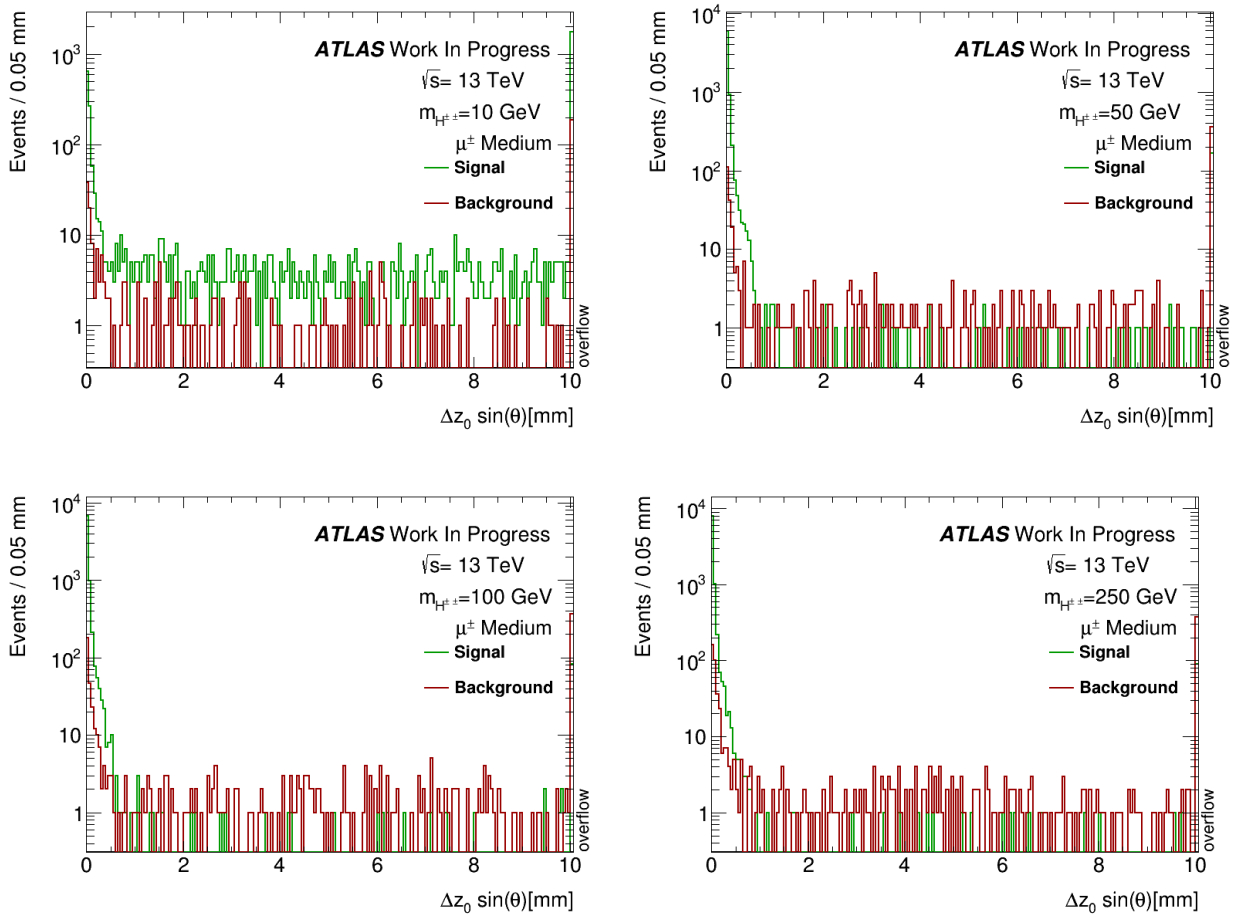

Figure 4.6: The $\Delta z_0 \sin(\theta)$ distribution is plotted with medium working point muons for the four different mass points. Histograms for both signal and background muons are plotted.

4.1.4 $\Delta\phi$ cut

The $\Delta\phi$ distributions for medium working point electrons are shown in figure 4.7. There is a clear peak around π for the signal-signal $\Delta\phi$ values due to the low boosted nature of the decay as mentioned in section 3.3. It is clear that a cut on $\Delta\phi$ around the π peak would be an effective tool in removing background with low reduction of signal events. The distributions are similar across mass points except the 10 GeV mass point where the low events passing the medium working point gives a statistical uncertainty. A $\Delta\phi$ cut between $\pi - 1$ and $\pi + 1$ was chosen as the cut for medium electrons and $\pi - 0.5$ and $\pi + 0.5$ for tight electrons.

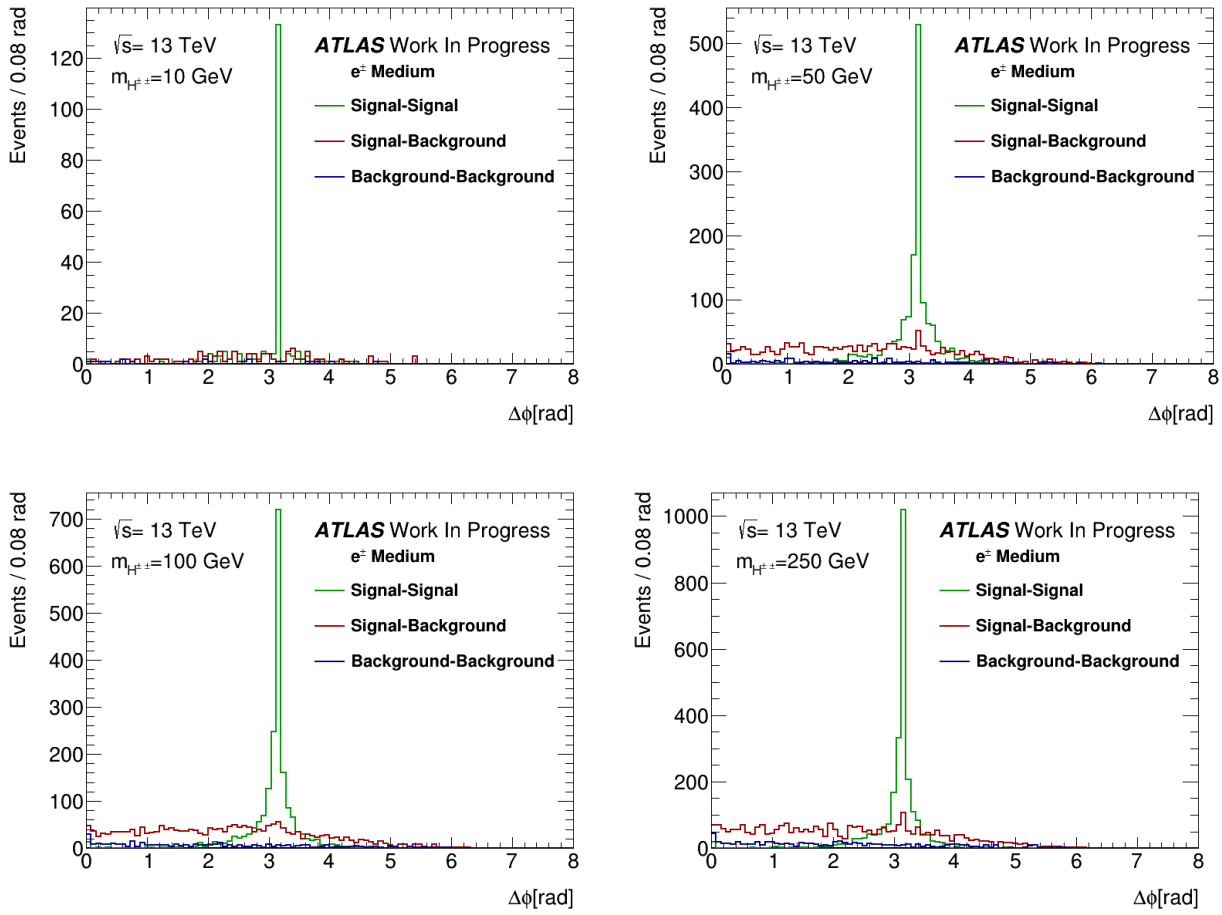

Figure 4.7: The $\Delta\phi$ distribution is plotted with medium working point electrons for the four different mass points. Three different histograms are stacked where $\Delta\phi$ is computed between two signal electrons, signal electrons and background electrons and two background electrons. The signal-signal electrons have a peak concentrated around π which have been used to remove background.

The $\Delta\phi$ distributions for medium working point muons are shown in figure 4.7. Three different histogram are overlapped with $\Delta\phi$ computed between two signal muons, signal and background muons and two background muons. There is a clear peak around π for muons similar to electrons. For muons there is quite a low amount of background muons so a cut on $\Delta\phi$ would not be as effective as for electrons but could reduce some background muons. The distribution is very similar across the different mass points with the exception of 10 GeV where the difference might be due to statistical uncertainty from the lower level of particles passing the medium working point. A $\Delta\phi$ cut between $\pi - 1$ and $\pi + 1$ was chosen as the cut for medium muons and $\pi - 0.5$ and $\pi + 0.5$ for tight muons.

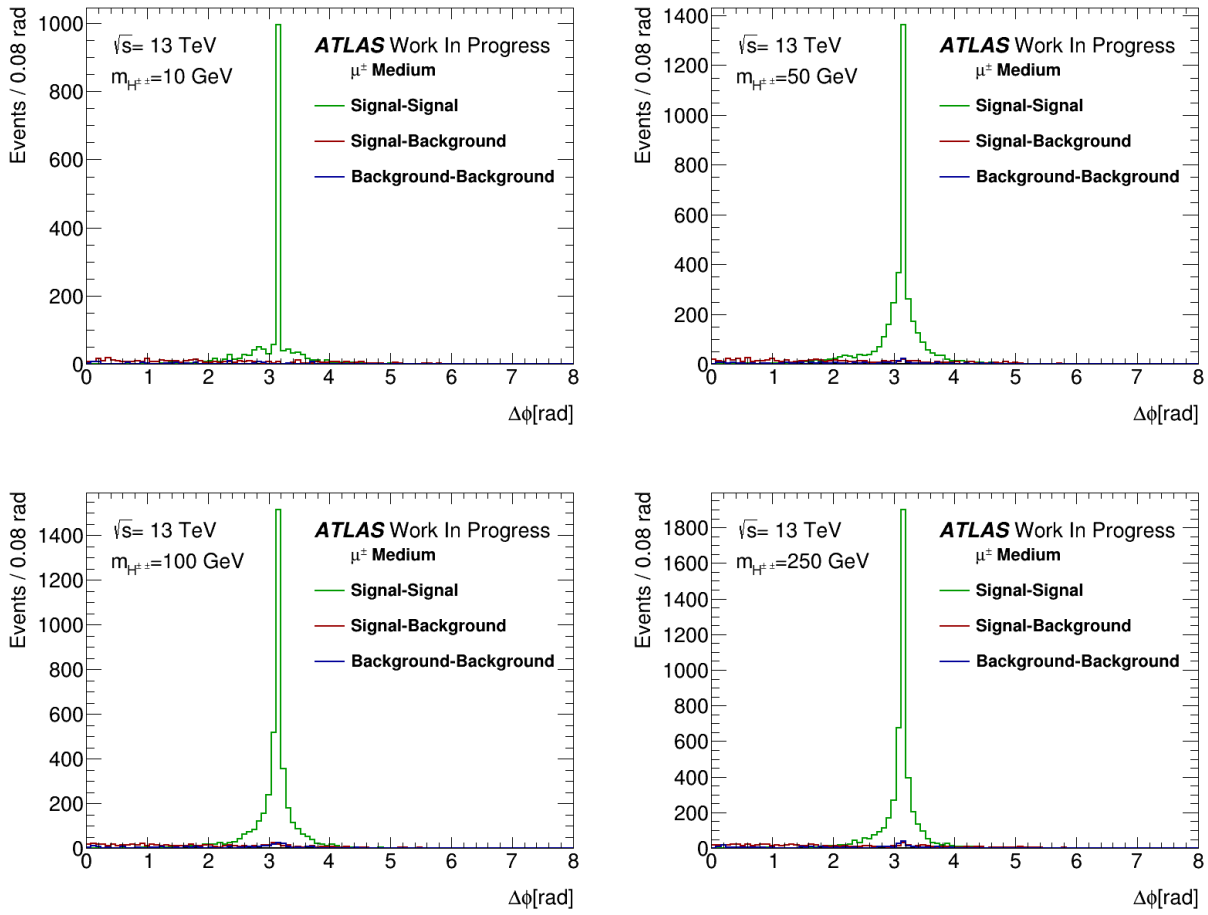

Figure 4.8: The $\Delta\phi$ distribution is plotted with medium working point muons for the four different mass points. Three different histograms are stacked where $\Delta\phi$ is computed between two signal muons, a signal muon and a background muon and two background muons. The signal-signal muons have a peak concentrated around π which have been used to remove background.

4.2 Event selection

4.2.1 Electrons

Electron candidates are reconstructed using the calorimetry and the ID by matching a charged track to an isolated electromagnetic calorimeter shower. The two selections used in this analysis, tight and medium, are summarized in table 4.3. These two selections were optimized to be a lower and upper estimate on the number of events passing. Electrons are required to be within the ID volume with $|\eta| < 2.5$. Electrons within the transition region($1.37 < |\eta| < 1.52$) of the barrel and endcap electromagnetic calorimeters are vetoed due to the reduced quality of the reconstruction in this area. Additionally, electrons are required to pass either the *LHMedium* or *LHTight* identification working point based on track and calorimeter information analyzed with a multivariate likelihood discriminant[36]. For isolation requirements

Table 4.3: Summary of the selection cuts used for electrons within this thesis. Two selection categories were set, one looser and one tighter to estimate a lower and upper limit.

Selection	Medium electrons	Tight electrons
Identification working point	*LHMedium*	*LHTight*
Isolation	*Loose_VarRad*	*Tight_VarRad*
η cut	$\lvert\eta\rvert < 1.37$ and $1.52 < \lvert\eta\rvert < 2.5$	$\lvert\eta\rvert < 1.37$ and $1.52 < \lvert\eta\rvert < 2.5$
$\lvert d_0\rvert/\sigma_{d_0}$ cut	None	$\lvert d_0\rvert/\sigma_{d_0} < 5.0$
$\lvert z_0 sin(\theta)\rvert$ cut	None	$\lvert\Delta z_0 sin(\theta)\rvert < 0.5$ mm
p_T cut	$p_T > 0$, 5, 10, 20 GeV	$p_T > 0$, 10, 15, 35 GeV
$\Delta\phi$ cut	$\pi - 1 < \Delta\phi < \pi + 1$	$\pi - 0.5 < \Delta\phi < \pi + 0.5$

the *Loose_VarRad* and *Tight_VarRad* working point was used that are further defined in Ref. [38]. Isolation uses calorimeter and track information around the electron candidate to veto if there is a large amount of hits around the candidate, where a looser cut on the hits is used for *Loose_VarRad*. Further, for tight electrons, the electron track impact parameter d_0, defined as the closest distance between the track and the beam axis in the transverse plane, must satisfies $|d_0|/\sigma_{d_0} < 5$ as explained in section 4.1.2. The track also needs to have a longitudinal impact parameter that satisfy $|\Delta z_0 sin(\theta)| < 0.5$ mm, where θ is the polar angle of the track and Δz_0 is the distance between the track and the primary vertex of the event in the z direction, with further information in section 4.1.3. Medium electrons were not required to satisfy this criterion due to it being an inefficient cut for the signal. For p_T cuts the cut is highly dependent on the mass point as the p_T distributions are very different. The p_T cuts are explained in section 4.1.1 and detailed in table 4.3. Due to the non-boosted nature of the signal a cut on $\Delta\phi$ was also implemented as explained in section 4.1.4.

4.2.2 Muons

Muons are reconstructed using information from the ID and muon spectrometer. In this analysis the selections used is summarized in table 4.4. Similarly to electrons, muons also have two selections, tight and medium, that are optimized to be a lower and upper estimate. Muons are required to be within $|\eta| < 2.5$ but are not vetoed between $(1.37 < |\eta| < 1.52)$ because the muon candidates do not shower in the calorimetry. The *LHMedium* and *LHTight* identification working point was used, which implements a multivariate likelihood discriminant described in Ref. [37]. For tight muons, the transverse impact parameter cut is set to $|d_0|/\sigma_{d_0} < 3.0$ and the longitudinal impact parameter cut is set to $|z_0 sin(\theta)| < 0.5$ mm. Medium muons were not required to satisfy this criterion due to it being an inefficient cut for the signal as mentioned in section 4.1.3. The isolation working point is set to the either *PflowTight_FixedRad* or *PflowLoose_FixedRad* which are further defined in Ref. [38]. Pflow isolation combines track and muon spectrometer information around the muon candidate to veto on the whole object if there is a large amount of hits around the candidate, where a looser cut on the hits is used for *PflowLoose_FixedRad*. The p_T cuts are covered in section 4.1.1 and $\Delta\phi$ cuts are explained in section 4.1.4.

Table 4.4: Summary of the selection cuts used for muons within this thesis. Two selection categories were set, one loose and one tighter to give a lower and upper limit.

Selection	Medium muons	Tight muons
Identification working point	*LHMedium*	*LHTight*
Isolation	*PflowLoose_FixedRad*	*PflowTight_FixedRad*
η cut	$\|\eta\| < 2.5$	$\|\eta\| < 2.5$
$\|d_0\|/\sigma_{d_0}$ cut	None	$\|d_0\|/\sigma_{d_0} < 3.0$
$\|z_0 sin(\theta)\|$ cut	None	$\|\Delta z_0 sin(\theta)\| < 0.5$ mm
p_T cut	$p_T > 0$, 5, 7.5, 10 GeV	$p_T > 0$, 10, 12.5, 30 GeV
$\Delta\phi$ cut	$\pi - 1 < \Delta\phi < \pi + 1$	$\pi - 0.5 < \Delta\phi < \pi + 0.5$

4.2.3 Tauons

Tauons are especially problematic to reconstruct because they decay before entering the ID. Tauons can decay into electrons, muons and hadronically, the decay that is easiest to reconstruct as a tau with the ATLAS detector is the hadronic decay which occurs around 65% of the time. The electron and muon decays are not possible to reconstruct as a tau due to the difficulty of separating them from other electrons and muons. In a hadronic decay the tau decays into a tau neutrino and a combination of charged and neutral pions. The pions are the visible part of this decay and they shower in the hadronic calorimeter and are reconstructed using jet reconstruction detailed in Ref. [39]. The selection cuts used in this analysis is summarized in table 4.5. The tau identification is done using a recurrent neural network(RNN)[40] algorithm with the working point set to *RNNMedium*. Further, tauons are required to be within $|\eta| < 2.5$ and are vetoed within the transition region of the calorimeter $1.37 < |\eta| < 1.52$. A p_T cut of 20 GeV is used which is the lowest value recommended for the ATLAS reconstruction. 1 or 3 tracks are required to match with the hadronic shower, this is due to the hadronic tau decaying into either one or three charged pions. The absolute value of the sum of charges from the tracks is required to be 1. To reduce the background of electrons being identified as tauons a likelihood electron veto is used with *EleBDTLoose* chosen as the working point.

Table 4.5: Summary of the selection cuts used for tauons within this thesis.

Selection	Medium tauons
Identification working point	*RNNMedium*
p_T cut	$p_T > 20$ GeV
η cut	$\|\eta\| < 1.37$ and $1.52 < \|\eta\| < 2.5$
Track Selection	1 or 3 tracks
Charge	$\|Q\| = 1$
Electron rejection	*EleBDTLoose*

4.3 Triggering

Within this analysis there were problems with the amount of memory needed while running the trigger during the reconstruction step on the grid. Memory limits on grid jobs killed all the jobs attempted. Because of this problem the reconstruction step was done without the trigger. The trigger was then studied using information of the general trigger menu in 2018[41] and the trigger performance in Run 2 for electrons[42], muons[43] and tauons[44]. The main unprescaled triggers for 2018 data taking were chosen to be emulated. Unprescaled indicates that the trigger always triggers if the conditions are met, while prescaled triggers are scaled to only trigger for a fraction of the times that the conditions are met. The triggers used are described in table 4.6 together with the variables used.

Table 4.6: Table describes the variables used when manually emulating the HLT trigger. The p_T cut is set slightly over stated trigger values to account for inconsistent performance of the trigger cut. Isolation cuts are only applied to electrons or muons and track cuts are only applied to tauons.

Event	HLT Trigger	p_T Cut	Working point	Isolation(mu & ele)	Track Cut(tau)
1 mu	mu_50	52 GeV	*LHMedium*	None	None
1 iso mu	mu26_ivarmedium	27 GeV	*LHMedium*	$p_T^{iso}(\Delta R^{var} < 0.3)p_T < 0.07$	None
2 mu	mu22_mu8	23 & 9 GeV	*LHMedium*	None	None
2 mu	2mu14	15 GeV	*LHMedium*	None	None
1 ele	e60_lhmedium_nod0	61 GeV	*LHMedium*	None	None
1 iso ele	e26_lhtight_nod0_ivarloose	27 GeV	*LHTight*	$p_T^{iso}(\Delta R^{var} < 0.2)p_T < 0.1$	None
2 ele	2e17_lhvloose_nod0	18 GeV	*LHVeryLoose*	None	None
1 tau	tau160_medium1_tracktwo	170 GeV	*JET_BDT_IDMedium*	None	$1 \leq N_{charged}^{track} \leq 3$ & $N_{iso}^{track} \leq 1$
2 tau	tau80_medium1_tracktwo_ tau35_medium1_tracktwo	85 & 40 GeV	*JET_BDT_IDMedium*	None	$1 \leq N_{charged}^{track} \leq 3$ & $N_{iso}^{track} \leq 1$
1 ele & 1 mu	e7_lhmedium_nod0_mu24	8 & 25 GeV	*LHMedium*	None	None
1 ele & 1 mu	e17_lhloose_nod0_mu14	18 & 15 GeV	*LHLoose* & *LHMedium*	None	None
1 ele & 1 mu	e26_lhmedium_nod0_mu8	27 & 9 GeV	*LHMedium*	None	None
1 mu & 1 tau	mu14_ivarloose_ tau25_medium1_tracktwo	15 & 30 GeV	*LHMedium* & *JET_BDT_IDMedium*	$p_T^{iso}(\Delta R^{var} < 0.3)p_T < 0.16$	$1 \leq N_{charged}^{track} \leq 3$ & $N_{iso}^{track} \leq 1$
1 ele & 1 tau	e17_lhmedium_nod0_ivarloose_ tau25_medium1_tracktwo	18 & 30 GeV	*LHMedium* & *JET_BDT_IDMedium*	$p_T^{iso}(\Delta R^{var} < 0.2)p_T < 0.1$	$1 \leq N_{charged}^{track} \leq 3$ & $N_{iso}^{track} \leq 1$

For simulating triggers only the HLT part of the trigger was emulated and there might be variables not accounted for within this thesis that are included in the HLT trigger. The L1 trigger was not emulated due to not being able to access L1 level variables and the complexity of the trigger chain. This choice rests on the assumption that a lepton passing the HLT trigger would also have passed the L1 trigger. This is not entirely accurate even with the lower threshold for the L1 triggers due to the low resolution available in the L1 trigger level.

The p_T cut used in the emulation of trigger was set slightly above the trigger level. This was done to try to account for inefficiencies in the trigger, where the trigger cut does not behave as a direct step function. Therefore the average p_T cut of the leptons that pass the trigger will lie slightly above its threshold for real data. The continuous curve for the trigger efficiency is not emulated within this thesis and instead the trigger is treated as a step function with a higher cut.

The lower p_T 2 tau triggers have not been emulated in this thesis. These triggers are optimized for boosted tauons coming from the Higgs boson decay into $\tau^-\tau^+$. These triggers use information at L1 level to greatly reduce the rate. Restriction on the ΔR between the taus

and requirements of additional jets close to the taus are applied at L1 level. These triggers have lower p_T cuts than the *tau80_medium1_tracktwo_tau35_medium1_tracktwo* trigger at a approximate cut of $p_T = 40, 30$ GeV. Due to the non-boosted nature of the $H^{\pm\pm}$ decay not many events were expected to pass these triggers and therefore it was decided to not attempt to emulate these triggers.

Track selections were not included in the trigger for both electron and muon triggers. Potential cuts on d_0 and Δz_0 could have been implemented within the trigger. Unfortunately, due to a lack of information if these cuts were implemented and what the cuts would be, no cuts were used. In the electron trigger it is explicitly stated that d_0 is not used. In the selections detailed in section 4.2 track selection have been implemented in the tight case which would account for this uncertainty.

4.4 Uncertainties

The main source of uncertainty investigated in this thesis is the theoretical systematic uncertainty on the MadGraph cross section. These values are computed using the systematics Python module within MadGraph. The estimated uncertainties are given after varying the renormalization and factorisation scales. Additionally, the PDF is varied to estimate the uncertainty coming from the parton distribution set. These uncertainties are added in squares and assumed to be non-correlated. The uncertainty is dominated by the scale uncertainty over the PDF uncertainty, with the scale uncertainty varying between 70% and 25% and the PDF uncertainty between 17% and 2.78%.

Further, statistical uncertainty in the amount of events passing reconstruction is quite large depending on the number of events passing and is added to the final uncertainty on the events. Additionally, the uncertainty of 1.7% on the Run 2 luminosity is added and assumed to be the same at Run 3 and 4. Systematic uncertainties from reconstruction and identification are not accounted for. For triggering there is a large potential for error in the emulation of the trigger done manually. This is not a source of uncertainty and instead a potential error in the configuration and is therefore not included in any uncertainty estimation.

Chapter 5

Results

In this chapter the general results of the thesis will be described. The initial number of estimated events through cross section values from Madgraph will first be presented. Then the emulated trigger results will be shown followed by a short section talking about the reconstructed tauons. Finally, the reconstruction efficiencies will be detailed and discussed together with the final number of expected events.

5.1 Number of Events

The number of events expected after Run 2, 3 and 4 with cumulative integrated luminosity values is shown in figure 5.1 for both the signal process as well as quark(neutral current) and photon induced double production of the doubly charged Higgs($p + p \rightarrow H^{\pm\pm} + H^{\mp\mp}$). The integrated luminosity values used were 139 fb^{-1} at Run 2[45] and the estimated values of 400 and 1500 fb^{-1} after Run 3 and 4 from Ref. [46]. Model parameters for this plot are $\nu_D = 10^{-8}$ GeV and $m_{\nu 1} = 5 \cdot 10^{-2}$ eV. The cross section for the run 3 and 4 data points are generated within Madgraph5 using $\sqrt{s} = 14$ TeV. The drop in cross section from the proton induced process to the lepton induced is very large due to the low probability of leptons within the proton. With these model parameters a 100 GeV mass signal is not visible at Run 2 luminosity. Lower mass points could be detected depending on the analysis effectiveness.

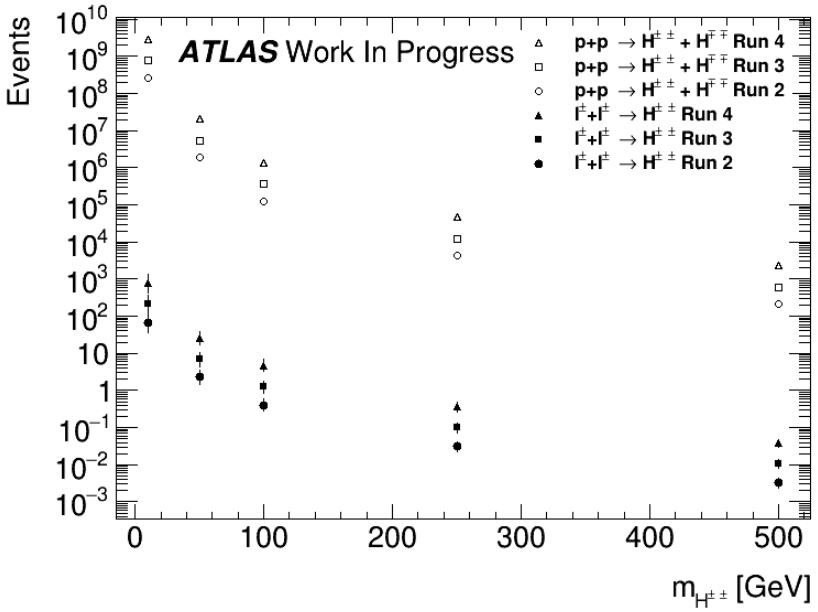

Figure 5.1: The number of events of the signal data set and proton-induced(photon and quark neutral current) double production of the doubly charged Higgs for run 2, 3 and 4 cumulative integrated luminosity plotted against the mass of the doubly charged Higgs. Cross section values for Run 3 and 4 are computed with $\sqrt{s} = 14$ TeV. Model parameters for this plot are set to $\nu_D = 10^{-8}$ GeV and $m_{\nu 1} = 5 \cdot 10^{-2}$ eV. There is a clear drop from the double production due to the low probability of leptons within the proton. The cross section is higher at low masses and decays quickly.

Figure 5.2 shows the cross sectional dependence on the model parameters ν_D and $m_{\nu 1}$ at Run 2 integrated luminosity. This shows that the cross section is highly dependent on the model parameters, mainly on the ν_D value where the cross section scales inversely as $1/\nu_D^2$. The dependence on $m_{\nu 1}$ is more complex with the difference between $5 \cdot 10^{-2}$eV and $5 \cdot 10^{-1}$eV being larger than between $5 \cdot 10^{-2}$eV to $5 \cdot 10^{-3}$eV. The more complex dependence comes from the mixing with the PMNS matrix as detailed in section 2.2. The minimum neutrino mass $m_{\nu 1}$ is also bound with the latest limit set at $m_\nu < 0.8$ eV 90% CL[47]. The dependence on the doubly charged Higgs mass is consistent across the different model parameters.

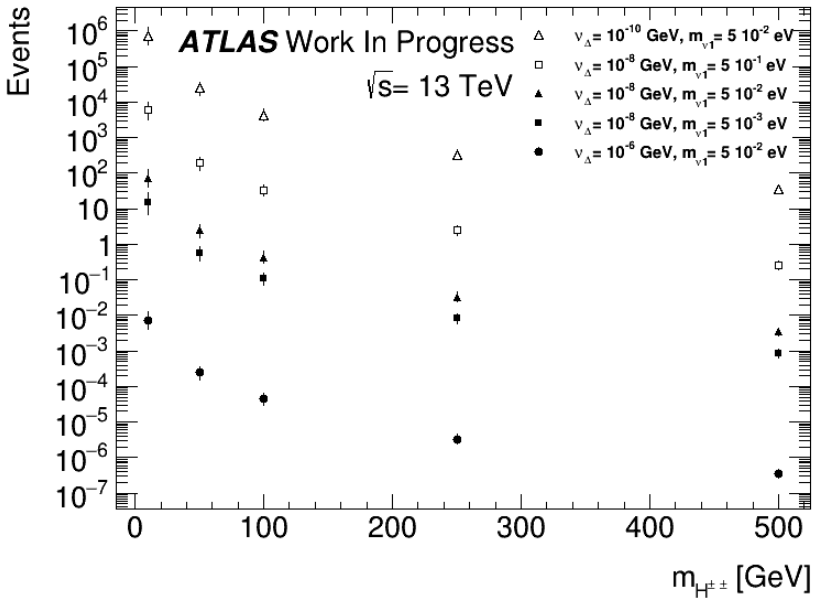

Figure 5.2: The number of events for the signal data set at Run 2 integrated luminosity with different values for ν_D and $m_{\nu 1}$ plotted against the mass of the doubly charged Higgs. The cross section has a large dependence on ν_D, it scales inversely as $\frac{1}{\nu_D^2}$. The dependence on the minimum neutrino mass is not as clear with a higher difference between $5 \cdot 10^{-2}$ and $5 \cdot 10^{-1}$ than between $5 \cdot 10^{-3}$ and $5 \cdot 10^{-2}$. The uncertainty includes combined statistical and systematic uncertainties detailed in section 4.4.

5.2 Triggering

The results from the emulating of the trigger described in section 4.3 is illustrated in figures 5.3, 5.4 and 5.5. Figure 5.3 shows the number of $H^{\pm\pm} \to e^{\pm} + e^{\pm}$ triggered events normalized to the total amount of events simulated for this decay process. Triggering varies greatly between mass points as expected from the p_T distributions. For $m_{H^{\pm\pm}} = 10$ GeV no trigger is passed due to the low p_T of the electrons from the decay. For the other triggers the 2e17(Table 4.6) and e26 triggers dominates as well as e60 for $m_{H^{\pm\pm}} = 250$ GeV. Not many of the non-electron triggers trigger except for the tau triggers at the high mass point. This might be due to electrons being mis-reconstructed as tauons instead.

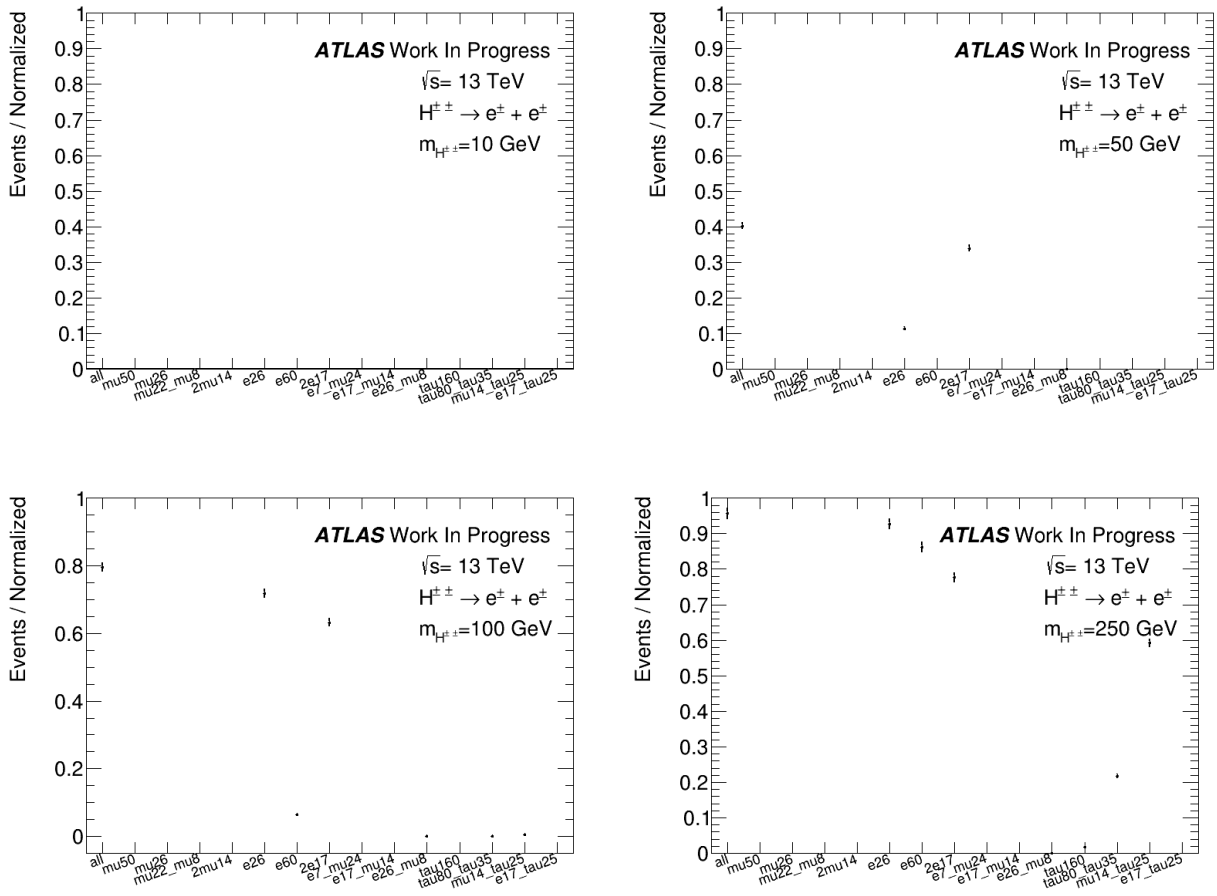

Figure 5.3: The triggering of events for $H^{\pm\pm} \to e^{\pm} + e^{\pm}$ normalized to the total events of the process is plotted for all the triggers. Trigger definitions are detailed in table 4.6. The lower mass points have much less events triggering with the higher mass almost triggering on every event. The error bars in the plot are only from statistical errors.

Figure 5.4 shows the number of triggers passing for $H^{\pm\pm} \to \mu^{\pm} + \mu^{\pm}$ events normalized to the total number of such events. The overall trigger efficiency varies with no events triggering at the $m_{H^{\pm\pm}} = 10$ GeV mass point to almost all at 250 GeV. The 2mu14(Table 4.6) and mu22_mu8 triggers dominate for $m_{H^{\pm\pm}} = 50$ GeV, with mu26, mu22_mu8 and 2mu14 all triggering for the higher mass points as well as mu50 for $m_{H^{\pm\pm}} = 250$ GeV.

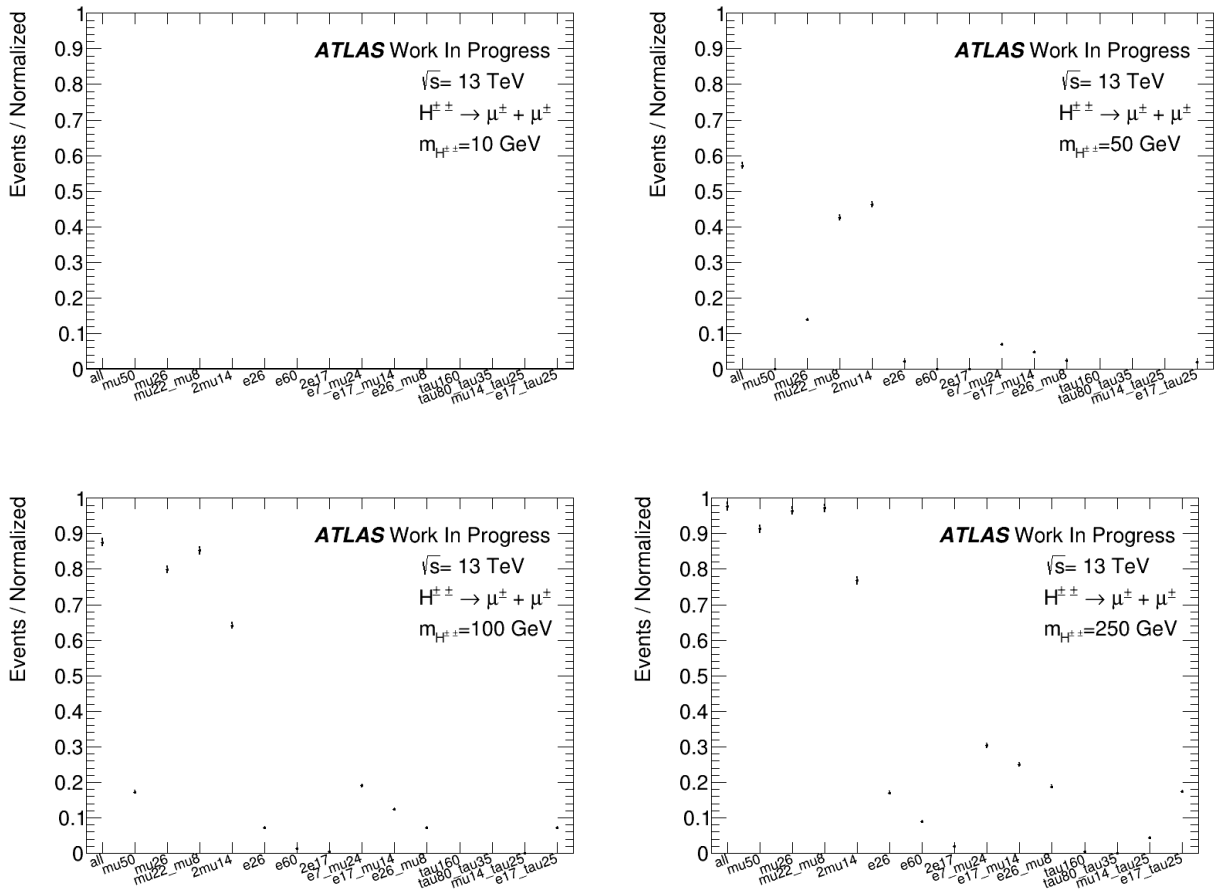

Figure 5.4: The triggering of events for $H^{\pm\pm} \to \mu^{\pm} + \mu^{\pm}$ normalized to the total events of the process is plotted for all the triggers. Trigger definitions are detailed in table 4.6. The lower mass points has much less events triggering with the higher mass triggering on every event. The error bars in the plot are only from statistical errors.

Figure 5.5 shows the number of triggers passing for $H^{\pm\pm} \to \tau^{\pm} + \tau^{\pm}$ events normalized to the total number of such events. The total number of passed events is very low for all mass points with an increase to around 0.55 at $m_{H^{\pm\pm}} = 250$ GeV. Which triggers that pass is quite inconsistent, with an even distribution over many triggers. Some of these triggers are from the electron and muon decays of the tau which are not possible to reconstruct as tauons and therefore will not be counted after event selection. The inclusion of the 2τ trigger described in section 4.3 could have improved the triggering especially due to its lower p_T cut but as mentioned not many events would potentially pass the ΔR cut.

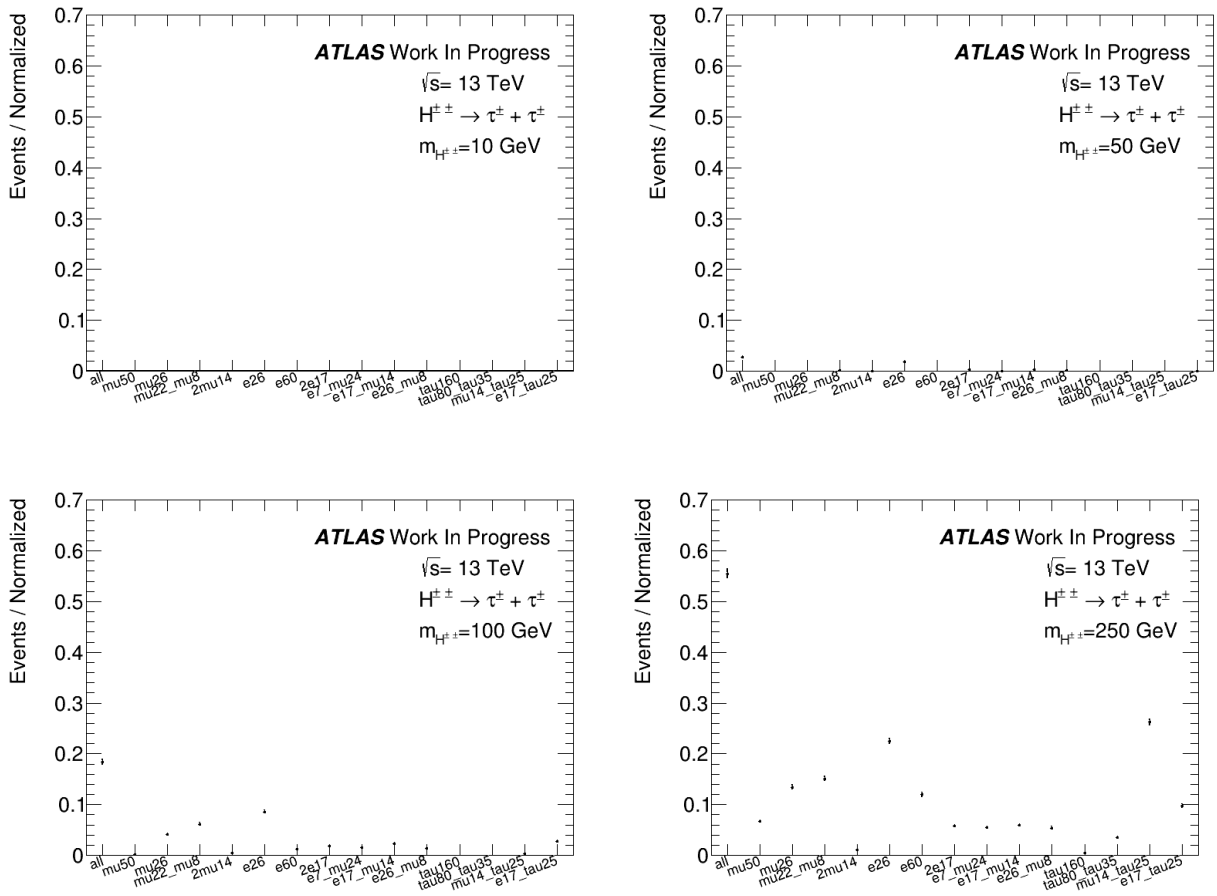

Figure 5.5: The triggering of events for $H^{\pm\pm} \to \tau^{\pm} + \tau^{\pm}$ normalized to the total events of the process is plotted for all the triggers. Trigger definitions are detailed in table 4.6. The lower mass points has much less events triggering. Interestingly, the muon triggers trigger much more than the tauon triggers. The error bars in the plot are only from statistical errors.

5.3 Tauons

For tauons the default p_T cut of 20 GeV means that for the lower mass points of $m_{H^{\pm\pm}} = 10, 50$ GeV close to all tauons are cut. Additionally, the trigger does not pass for many of these events. For the higher mass points the selection cuts does not eliminate as many events. The p_T distribution of medium selection tauons in events with more than two tauons is shown in figure 5.6. The distribution does not peak at $m_{H^{\pm\pm}}/2$ as in the true distribution in figure 3.2c. The probable cause of this is the energy carried away by the neutrino in the tau decay which is not detectable with the detector. The plotted p_T is calibrated to counteract this problem but it does not overcome the problem fully. There might be other calibrations that have not been done within this thesis but ultimately it was decided to not include tauons in the total count of good events due to the ineffective triggering and selection as well as the inconsistent p_T.

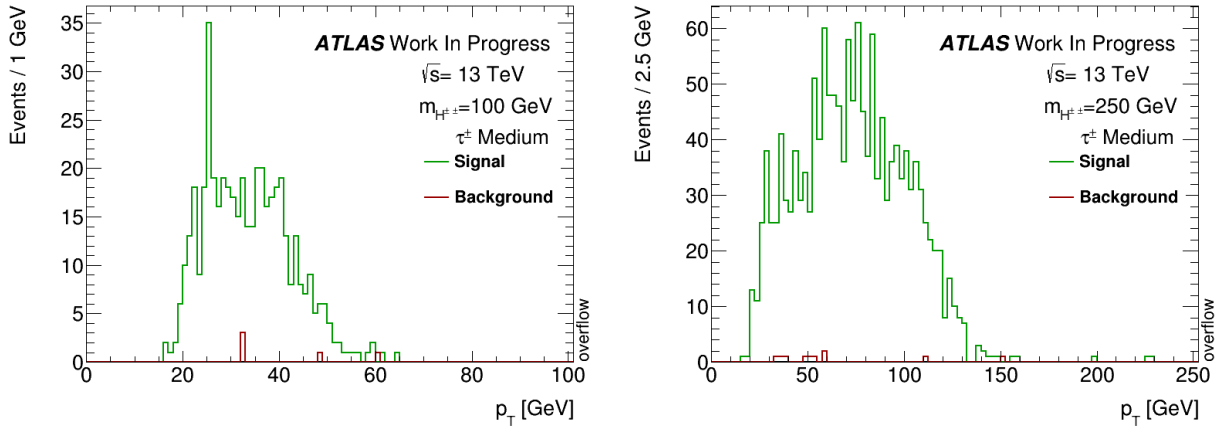

Figure 5.6: The p_T distribution is plotted for medium selection signal and background tauons for $m_{H^{\pm\pm}} = 100, 250$ GeV. Background rejection is very good for both mass points. The distribution is very inconsistent compared to the peak at $m_{H^{\pm\pm}}/2$ for simulation truth.

5.4 Final number of events

A final event is required to have two same-sign charged leptons of the same flavour. Both leptons have to pass the selections mentioned in section 4.2. The event also have to pass the emulated trigger detailed in section 4.3 with the triggers passing shown in section 5.2. For an event to pass the trigger any trigger passed will be counted, even triggers that do not correspond to the event signal. The event might still have additional background leptons in the event that also passes the selection cuts.

The number of passed signal events were computed for the different selection working points and are given in table 5.1. In parenthesis is the percentage of events passing the selection out of the total for that process as given figure 3.3. Table 5.2 show the number of background events where two selected leptons are present but less than 2 are signal leptons. In parenthesis is the number of background events divided by the total number of selected events. Due to no events triggering at 10 GeV no final events remain across the different lepton categories. The muon signal is the best performing with high selection and low background, which is expected due to the excellent reconstruction at ATLAS. Electrons perform worse with a larger amount of background electrons and lower selection but still reaches 53.65% for medium electrons at $m_{H^{\pm\pm}} = 250$ GeV. The amount of events with background electrons selected is rather high varying between 10%-17% out of the total selected events. There is between around 1100 and 600 events difference between medium and tight muons, while for electrons the difference in the number of events vary between 500 and 700. Tauons perform worst which mainly is due to the inefficient triggering as well as the problems with reconstructing taus.

Table 5.1: The number of final simulated events with two signal leptons passing the selections is given for the different type of leptons and mass points. In the parenthesis is the value divided by the total number of events for the specific lepton process from figure 3.3. Due to no events triggering there are no final events for the 10 GeV mass point.

Mass Point	Medium $e^{\pm}e^{\pm}$	Tight $e^{\pm}e^{\pm}$	Medium $\mu^{\pm}\mu^{\pm}$	Tight $\mu^{\pm}\mu^{\pm}$	Medium $\tau^{\pm}\tau^{\pm}$
$m_{H^{\pm\pm}} = 10$ GeV	0	0	0	0	0
$m_{H^{\pm\pm}} = 50$ GeV	806±28(20.5%)	316±18(8.03%)	2789±53(44.7%)	1652±41(26.5%)	0
$m_{H^{\pm\pm}} = 100$ GeV	1573±40(38.7%)	895±30(22.0%)	3735±61(61.2%)	2862±53(46.9%)	25±5.0(0.460%)
$m_{H^{\pm\pm}} = 250$ GeV	2154±46(53.7%)	1632±40(40.7%)	4417±66(72.7%)	3795±62(62.5%)	446±21(8.01%)

Table 5.2: The number of final simulated events passing the final selection but with at least one background lepton instead of two signal leptons. In parenthesis is the value divided by the total number of events passing the selection. The number of background events is quite low for muons and rather high for electrons.

Mass Point	Medium $e^{\pm}e^{\pm}$	Tight $e^{\pm}e^{\pm}$	Medium $\mu^{\pm}\mu^{\pm}$	Tight $\mu^{\pm}\mu^{\pm}$	Medium $\tau^{\pm}\tau^{\pm}$
$m_{H^{\pm\pm}} = 10$ GeV	0	0	0	0	0
$m_{H^{\pm\pm}} = 50$ GeV	145±12(15.4%)	48±6.9(13.2%)	15±3.9(0.535%)	3±1.7(0.181%)	0
$m_{H^{\pm\pm}} = 100$ GeV	319±18(16.9%)	113±11(11.2%)	59±7.7(1.56%)	61±7.8(2.09%)	2±1.4(7.41%)
$m_{H^{\pm\pm}} = 250$ GeV	403±20(15.8%)	181±13(9.98%)	110±10(2.43%)	28±5.3(0.732%)	6±2.4(1.33%)

Table 5.3 show the fraction of the number of signal final events over the total simulated events(16000). Only muons and electrons are included in these counts due to the poor p_T reconstruction of tauons. Medium electrons and muons are combined into medium events and tight electron and muons are combined into tight events. There is approximately a 0.1 difference between the tight and medium selection at $m_{H^{\pm\pm}} = 50, 100$ GeV, while for $m_{H^{\pm\pm}} = 250$ GeV the difference is around 0.7.

Table 5.3: The ratio of final simulated signal events over the total 16000 events generated for the medium and tight selections. This only includes electron and muons due to the poor p_T reconstruction of tauons.

Mass Point	Medium Events	Tight Events
$m_{H^{\pm\pm}} = 10$ GeV	0	0
$m_{H^{\pm\pm}} = 50$ GeV	0.225±0.004	0.123±0.0028
$m_{H^{\pm\pm}} = 100$ GeV	0.332±0.005	0.235±0.004
$m_{H^{\pm\pm}} = 250$ GeV	0.411±0.005	0.340±0.005

The fractions given in table 5.3 are used in figures 5.7 and 5.8 to give the final estimation of the number of events possible to detect at ATLAS. Figure 5.7 plot the number of tight and medium events for run 2, 3 and 4 cumulative integrated luminosities with model parameters set to $\nu_D = 10^{-8}$ GeV and $m_{\nu 1} = 5 \cdot 10^{-1}$ eV. For the 500 GeV data point the fraction from the 250 GeV mass point is used. The number of events is low for all mass points with run 2 values all being lower than 1 event.

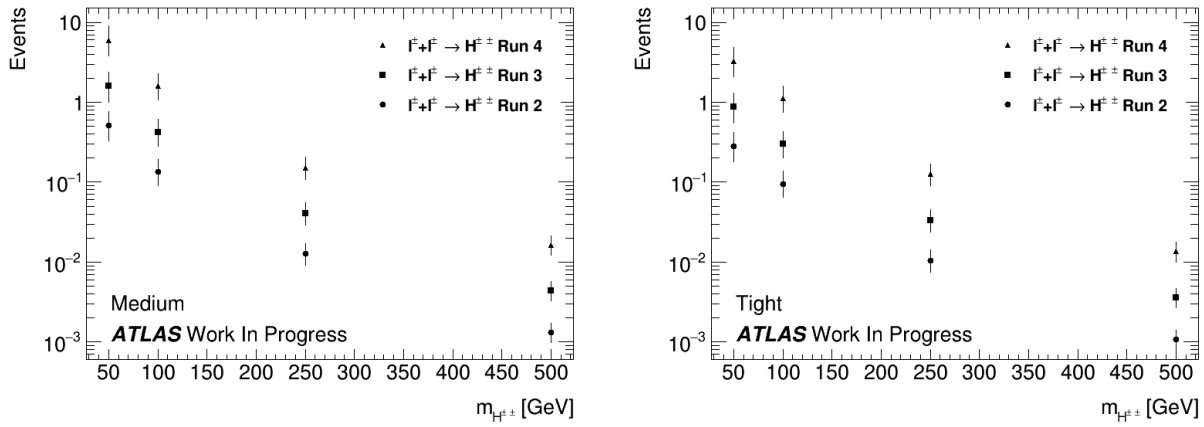

Figure 5.7: The final number of signal events after factoring in the medium and tight ratio of reconstructed events in table 5.1 is plotted for Run 2, 3 and 4 integrated luminosity values. For the 500 GeV data point the same ratio is used as for 250 GeV. In this plot the cross section is computed using $\nu_D = 10^{-8}$ GeV and $m_{\nu 1} = 5 \cdot 10^{-2}$ eV. The number of events are low at all mass ranges with no mass point being observable at Run 2 luminosity with these values. The uncertainties of the data points are explained in section 4.4.

As seen in section 5.1 the number of events is highly dependent on model parameters, this is shown in figure 5.8 at Run 2 integrated luminosity. If the minimum neutrino mass is increased to $m_{\nu 1} = 5 \cdot 10^{-1}$ eV the cross section could increase up to approximately $39.56^{+19.60}_{-14.17}$ events at a 50 GeV mass point. A vacuum expectation value ν_D of 10^{-10} GeV would increase the number of events substantially to $5.12^{+2.579}_{-1.860} \cdot 10^3$ at 50 GeV and $13.17^{+4.094}_{-3.376}$ at 500 GeV. A lower ν_D value would decrease the number of events to under 10^{-4} for all masses, for low ν_D values this signal would not be possible to detect at ATLAS. Importantly, there is a upper limit set on the ν_D value within this thesis where the charged lepton branching ratio of the doubly charged Higgs dominate at values lower than 10^{-4}. For higher ν_D the W-boson decay needs to be studied instead or a combination of the two. As mentioned in section 5.1 there is an upper limit on the minimum neutrino mass from experimental measurements at $m_\nu < 0.8$ eV at 90% confidence level[47]. The highest value used in this thesis of $5 \cdot 10^{-1}$ eV is therefore close to this limit.

The $p + p \rightarrow H^{\pm\pm} + H^{\mp\mp}$ process does not have as large of a dependence on ν_D as $\ell^{\pm} + \ell^{\pm} \rightarrow H^{\pm\pm}$. This means that for $\nu_D < 10^{-10}$ GeV the lepton-initiated process might become dominant over the other processes. This occurs at approximately $5 \cdot 10^{-12}$ using quark(neutral current) and photon fusion for the $p + p \rightarrow H^{\pm\pm} + H^{\mp\mp}$ process. In this parameter space the lepton-initiated process will be very important.

The use of the ratio simulated at 250 GeV for the 500 GeV data point was done due to a focus on the lower mass range. This is a simplification which is not necessarily an accurate approximation. There is no increase possible in the trigger as can be seen in the 250 GeV plots in section 5.2, with close to all events already triggering for electrons and muons. An increase in the factor should be expected at a higher mass point due to more efficient background

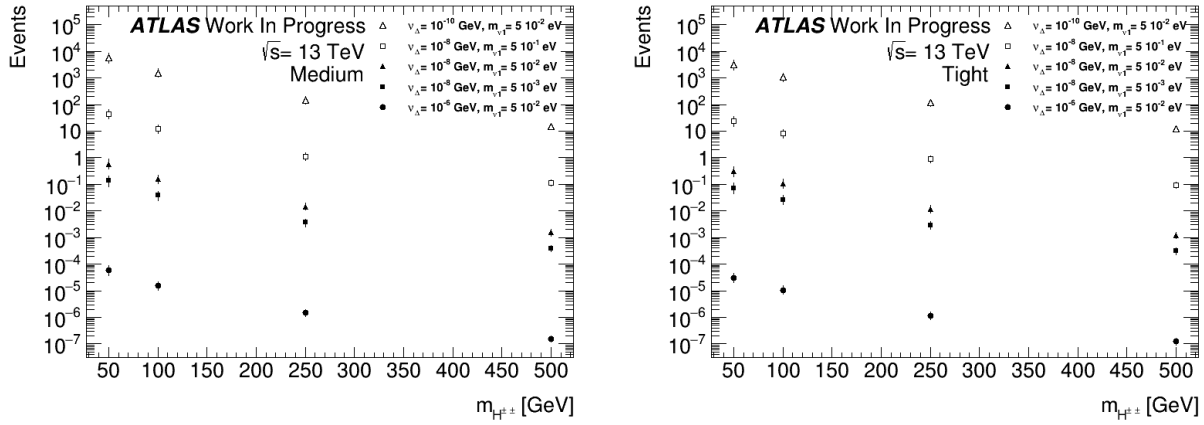

Figure 5.8: The final number of signal events after factoring in the ratio of reconstructed events is plotted with different model parameters for Run 2 integrated luminosity. For the 500 GeV data point the same ratio is used as for 250 GeV. The cross section is highly dependent on these values as can be seen by the large difference in events. The uncertainties of the data points are explained in section 4.4.

removal and a more narrow η distribution but the difference will be smaller between high mass points. At p_T's above 300 GeV the *highPt* WP is recommended to be used instead of *LHMedium*, which could affect the reconstruction efficiency.

The cumulative integrated luminosity values for run 3 and 4 are estimations of what might be obtained and are subject to change depending on the operation of the LHC. Further, the reconstruction factor estimated in this thesis for Run 2 settings might be different at future runs. Improvements in hardware of the detector and changes in reconstruction algorithms might be able to improve this factor, while future triggers might eliminate more events at low p_T by increasing the p_T cuts.

The largest uncertainty of the final values is by far the systematic uncertainty of the cross section from Madgraph. To decrease this systematic uncertainty one could simulate the process at Next to Leading Order(NLO) instead of LO as used within this thesis. A previous study[48] into similar lepton-induced processes has shown a significant decrease in uncertainty from $\mathcal{O}(50\%)$ at LO to $\mathcal{O}(10\%)$ at NLO. Some small differences in p_T of the scalar particle was also observed which could have a small effect on the study in this thesis.

The largest potential source of uncertainty and error not calculated in this thesis might be the emulated trigger. Only attempting to emulate the HLT trigger level ignores a lot of the inefficiency present at L1 level. With the treatment of the trigger as a step function and with full efficiency for p_T's above the cut, the trigger efficiency was ignored within this thesis. For the unprescaled single muon triggers the maximum trigger efficiency from $Z \to \mu\mu$ events is ≈ 0.7 for $|\eta| < 1.05$ and ≈ 0.87 for $1.05 < |\eta| < 2.5$ with slight difference between data periods. For the mu14(Table 4.6) trigger the maximum trigger efficiency from $Z \to \mu\mu$ events is ≈ 0.75 for $|\eta| < 1.05$ and ≈ 0.85 for $1.05 < |\eta| < 2.5$ with small difference between data periods. For the combined single electron triggers the maximum efficiency is close to $\approx$0.97,

while close to the trigger cut the efficiency is a lower ≈0.75. For dielectron triggers the trigger efficiency varies between the maximum of ≈0.97 to the lower bound of ≈0.55. By combining all the triggers for a certain process the efficiency might increase overall above the stated values here. It is also not clear if the selection used within this thesis might exclude some of the leptons that would not trigger due to these trigger inefficiencies. Overall, the complexity of these efficiencies meant that they were not emulated within this thesis, the efficiencies should lead to a lower number of triggered events than what has been emulated but the effect is hard to quantify.

An important factor missing within the scope of this thesis is applying scale factor to the MC data. Due to differences between MC and real data at ATLAS there exists calibrated scale factor that scales different variables from MC to match the proper values observed with the detector. These factors are usually on the order of a few percent but it is of course important to properly investigate their actual effect with this signal. For a general analysis of the signal process, the isolation working point should be investigated. Within this thesis there was not enough time to determine the best performing isolation but the optimal performance should be between the medium and tight selection.

As detailed in section 3.2 only $e^{\pm} + e^{\pm} \rightarrow H^{\pm\pm}$ events were used in the simulation. Being able to use muons and tauons in the initial state would increase the p_T of the decay products. This would potentially lead to a small increase in triggering and efficiency in the p_T cut. A boosted signal would on the other hand potentially lower the efficiency in $\Delta\phi$ cuts where a more boosted decay would lead to a broader distribution.

Only the potential background to the signal from pile-up leptons within the event was estimated in this thesis. For muons the percentage of events with background muons in the final selection varied between 0.2% and 2.5% for tight and medium muons. For electrons the percentage varies between 10% and 17% for tight and medium electrons. The main potential sources of background could be prompt leptons from diboson and $t\bar{t}$ events as well as non-prompt background from various sources but mainly charge misidentification. Additionally, lepton-lepton scattering is enabled by the lepton PDFs which could be a large background depending on its characteristics compared to the DCH signal. The $\Delta\phi$ distribution should be a powerful tool to remove some of this background but the low number of signal events observable at ATLAS and the very large cross section for some of the background processes means that a substantial amount of background events could drown out the signal.

From the general study of the doubly charged Higgs at ATLAS[12] the total expected background at $m_{H^{\pm\pm}}$ = 300-1300 GeV was 40 $\pm$ 5 events for $e^{\pm}e^{\pm}$ and 14.8 $\pm$ 1.6 $\mu^{\pm}\mu^{\pm}$ signals. This is an approximation of what background to be expected for the signal studied within this thesis. With a cleaner signal with the $\ell^{\pm} + \ell^{\pm} \rightarrow H^{\pm\pm}$ process there is potential to reduce this background through $\Delta\phi$ cuts for example.

The recent study of the doubly charged Higgs at ATLAS in Ref. [12] did not find any significant evidence for the signal. The combined limit on the $H^{\pm\pm}$ mass was found to be 1080 GeV. This limit excludes the mass points used within this thesis. The signal used within this thesis could potentially add to this search depending on the potential background and model parameter space. The proton-induced production process would be the dominant signal

process but at certain model parameters, especially $\nu_D < 10^{-10}$ GeV the lepton production might become more dominant. In a model where the doubly charged Higgs would only couple to leptons the signal within this thesis would be only process to observe at the LHC. Within my knowledge there is no model limiting the coupling of the doubly charged Higgs in this way. Within this scenario there are also limits from the experiments at the Large Electron-Positron Collider(LEP)[49, 50, 51] which have limits set between 95.5 and 98.5 GeV at 95% CL. These limits are as well model dependent and theory development since then might also have an effect on the limits.

Chapter 6

Summary and Outlook

The aim of this thesis is to give an estimate of the number of events of the $\ell^{\pm} + \ell^{\pm} \rightarrow H^{\pm\pm}$ process observable with the ATLAS detector. The thesis has focused on the subsequent decay into charged leptons which becomes dominant for ν_D lower than 10^{-4}. To estimate the number of events, the cross section has been computed through Madgraph5. Triggering, reconstruction and selection efficiencies at ATLAS have been analysed. The final events have been calculated for Run 2, 3 and 4 cumulative integrated luminosity and for different model parameters.

Simulation of the process at LO with $\sqrt{s} = 13$ TeV was performed using Madgraph5, Herwig and EvtGen. 16000 events were simulated using the type-II seesaw model and lepton parton distributions functions. Simulation and Reconstruction was done following the MC16 campaign and using ATLFastII. Due to problems with the parton showering only $e^{\pm} + e^{\pm} \rightarrow H^{\pm\pm}$ events were used. Different reconstruction cuts including p_T, d_0, $\Delta z_0 sin(\theta)$ and $\Delta\phi$ were investigated. A tight selection and a medium one was used for electrons and muons, while for tauons only a medium selection was used.

Due to memory problems while running the trigger within the reconstruction at ATLAS, the triggering was emulated manually. Charged lepton HLT triggers were chosen to be emulated with cuts on p_T, isolation, track parameters and working points. The trigger performs very differently between mass points with no events triggering at 10 GeV and close to all triggering in $e^{\pm}e^{\pm}$ and $\mu^{\pm}\mu^{\pm}$ events at 250 GeV.

The final number of events expected was computed for different model parameters and cumulative integrated luminosity values for Run 2, 3 and 4. The number of observable events is overall low with more events at low ν_D and high $m_{\nu 1}$. For $\nu_D = 10^{-8}$ GeV and $m_{\nu 1} = 5 \cdot 10^{-2}$ eV lower than 1 event is observable at Run 2 for all mass points. For Run 3 and Run 4 fewer than 10 events are observable at $m_{H^{\pm\pm}} = 50, 100$ GeV. For $\nu_D < 10^{-10}$ GeV the lepton-induced process might become competitive with the proton-induced one.

Several parts need to be improved on for a full analysis, solving the problems with simulating muons in the initial state would give a definitive result without assuming the extension from $e^{\pm} + e^{\pm} \rightarrow H^{\pm\pm}$. Solving the memory problems with simulating the trigger should be a

priority, with the emulated trigger potentially missing several details which could change the results, especially the trigger efficiencies. Scale factors should be implemented to get a proper comparison between MC and data. Finally, background should be properly estimated where diboson, $t\bar{t}$, charge misidentification and lepton-lepton scattering are expected to be the dominant backgrounds.

Acknowledgments

Firstly, I would like to extend my sincerest thanks to my supervisor Prof. Else Lytken for her continuing support. Especially due to the difficult situation of working from home at certain parts of the year. I would also like to thank Nathan Simpson for giving support and input. Finally, I am grateful for the continuous support from friends, family and girlfriend.

Bibliography

1. Evans L and Bryant P. LHC Machine. Journal of Instrumentation 2008 Aug; 3:S08001–S08001. DOI: 10.1088/1748-0221/3/08/s08001
2. ATLAS collaboration. The ATLAS Experiment at the CERN Large Hadron Collider. JINST 2008; 3:S08003. 437 p. DOI: 10.1088/1748-0221/3/08/S08003
3. ATLAS collaboration. Observation of a new particle in the search for the Standard Model Higgs boson with the ATLAS detector at the LHC. Physics Letters B 2012; 716:1–29. DOI: https://doi.org/10.1016/j.physletb.2012.08.020
4. Pati JC and Salam A. Lepton number as the fourth "color". Phys. Rev. D 1974 Jul; 10(1):275–89. DOI: 10.1103/PhysRevD.10.275
5. Mohapatra RN and Pati JC. Left-right gauge symmetry and an "isoconjugate" model of CP violation. Phys. Rev. D 1975 Feb; 11(3):566–71. DOI: 10.1103/PhysRevD.11.566
6. Senjanovic G and Mohapatra RN. Exact left-right symmetry and spontaneous violation of parity. Phys. Rev. D 1975 Sep; 12(5):1502–5. DOI: 10.1103/PhysRevD.12.1502
7. Fuks B, Nemevšek M, and Ruiz R. Doubly charged Higgs boson production at hadron colliders. Physical Review D 2020 Apr; 101. DOI: 10.1103/physrevd.101.075022
8. Corcella G, Corianò C, Costantini A, and Frampton PH. Exploring scalar and vector bileptons at the LHC in a 331 model. Physics Letters B 2018 Oct; 785:73–83. DOI: 10.1016/j.physletb.2018.08.015
9. Zee A. Quantum numbers of Majorana neutrino masses. Nuclear Physics B 1986; 264:99–110. DOI: https://doi.org/10.1016/0550-3213(86)90475-X
10. Babu K. Model of "calculable" Majorana neutrino masses. Physics Letters B 1988; 203:132–6. DOI: https://doi.org/10.1016/0370-2693(88)91584-5
11. Georgi H and Machacek M. Doubly charged Higgs bosons. Nuclear Physics B 1985; 262:463–77. DOI: https://doi.org/10.1016/0550-3213(85)90325-6
12. ATLAS collaboration. Search for doubly charged Higgs boson production in multi-lepton final states using $139\,\text{fb}^{-1}$ of proton–proton collisions at $\sqrt{s} = 13\,\text{TeV}$ with the ATLAS detector. Tech. rep. Geneva: CERN, 2022 Mar. Available from: https://cds.cern.ch/record/2805214
13. Buonocore L, Nason P, Tramontano F, and Zanderighi G. Leptons in the proton. Journal of High Energy Physics 2020 Aug; 2020. DOI: 10.1007/jhep08(2020)019

14. Martin B and Shaw. G. Particle Physics. 3rd ed. John Wiley & Sons, 2008. DOI: 10.1140/epjc/s10052-018-5661-z

15. Lubej M. Available from: https://www.physik.uzh.ch/groups/serra/StandardModel.html [Accessed on: 2022 Jan 25]

16. Kane G. Modern Elementary Particle Physics: Explaining and Extending the Standard Model. 2nd ed. Cambridge University Press, 2017. DOI: 10.1017/9781316691434

17. Griffiths D. Introduction to Elementary Particles. Physics textbook. Wiley, 2008. Available from: https://books.google.se/books?id=Wb9DYrjcoKAC

18. CMS Collaboration. Observation of a new boson at a mass of 125 GeV with the CMS experiment at the LHC. Physics Letters B 2012; 716:30–61. DOI: https://doi.org/10.1016/j.physletb.2012.08.021

19. Particle Data Group. Review of Particle Physics. Progress of Theoretical and Experimental Physics 2020 Aug; 2020. DOI: 10.1093/ptep/ptaa104

20. Fileviez Pérez P, Han T, Huang G, Li T, and Wang K. Neutrino masses and the CERN LHC: Testing the type II seesaw mechanism. Physical Review D 2008 Jul; 78. DOI: 10.1103/physrevd.78.015018

21. Martin AD, Stirling WJ, Thorne RS, and Watt G. Parton distributions for the LHC. The European Physical Journal C 2009 Jul; 63:189–285. DOI: 10.1140/epjc/s10052-009-1072-5

22. Manohar A, Nason P, Salam GP, and Zanderighi G. How Bright is the Proton? A Precise Determination of the Photon Parton Distribution Function. Physical Review Letters 2016 Dec; 117. DOI: 10.1103/physrevlett.117.242002

23. Manohar AV, Nason P, Salam GP, and Zanderighi G. The photon content of the proton. Journal of High Energy Physics 2017 Dec; 2017. DOI: 10.1007/jhep12(2017)046

24. Mobs E. The CERN accelerator complex - 2019. 2019 Jul. Available from: https://cds.cern.ch/record/2684277

25. Alemany-Fernandez R et al. Operation and Configuration of the LHC in Run 1. 2013 Nov. Available from: https://cds.cern.ch/record/1631030

26. Wenninger J. Operation and Configuration of the LHC in Run 2. 2019 Mar. Available from: https://cds.cern.ch/record/2668326

27. ATLAS collaboration. Operation of the ATLAS trigger system in Run 2. Journal of Instrumentation 2020 Oct; 15:P10004–P10004. DOI: 10.1088/1748-0221/15/10/p10004

28. Alwall J et al. The automated computation of tree-level and next-to-leading order differential cross sections, and their matching to parton shower simulations. Journal of High Energy Physics 2014 Jul; 2014. DOI: 10.1007/jhep07(2014)079

29. Bierlich C, Chakraborty S, Desai N, Gellersen L, Helenius I, Ilten P, Lönnblad L, Mrenna S, Prestel S, Preuss CT, Sjöstrand T, Skands P, Utheim M, and Verheyen R. A comprehensive guide to the physics and usage of PYTHIA 8.3. 2022. DOI: 10.48550/ARXIV.2203.11601

30. Bähr M et al. Herwig physics and manual. The European Physical Journal C 2008 Nov; 58:639–707. DOI: 10.1140/epjc/s10052-008-0798-9

31. Bellm J et al. Herwig 7.0/Herwig++ 3.0 release note. Eur. Phys. J. C 2016; 76:196. DOI: 10.1140/epjc/s10052-016-4018-8

32. Lange DJ. The EvtGen particle decay simulation package. Nucl. Instrum. Meth. A 2001; 462. Ed. by Erhan S, Schlein P, and Rozen Y:152–5. DOI: 10.1016/S0168-9002(01)00089-4

33. Agostinelli S et al. Geant4—a simulation toolkit. Nuclear Instruments and Methods in Physics Research Section A: Accelerators, Spectrometers, Detectors and Associated Equipment 2003; 506:250–303. DOI: https://doi.org/10.1016/S0168-9002(03)01368-8

34. Wolfgang L. (for the ATLAS Collaboration). Fast Simulation for ATLAS: Atlfast-II and ISF. Tech. rep. Geneva: CERN, 2012 Jun. DOI: 10.1088/1742-6596/396/2/022031

35. Yamanaka T. (for the ATLAS Collaboration). The ATLAS calorimeter simulation FastCaloSim. Journal of Physics: Conference Series 2011 Dec; 331:032053. DOI: 10.1088/1742-6596/331/3/032053

36. ATLAS Collaboration. Electron reconstruction and identification in the ATLAS experiment using the 2015 and 2016 LHC proton-proton collision data at $\sqrt{s} = 13$ TeV. The European Physical Journal C 2019 Aug; 79. DOI: 10.1140/epjc/s10052-019-7140-6

37. ATLAS Collaboration. Muon reconstruction and identification efficiency in ATLAS using the full Run 2 *pp* collision data set at $\sqrt{s} = 13$ TeV. Eur. Phys. J. C 2021; 81:578. DOI: 10.1140/epjc/s10052-021-09233-2

38. Recommended isolation working points (Rel. 21). https://twiki.cern.ch/twiki/bin/view/AtlasProtected/RecommendedIsolationWPs. Accessed: 2022-02-30

39. ATLAS Collaboration. Reconstruction, Energy Calibration, and Identification of Hadronically Decaying Tau Leptons in the ATLAS Experiment for Run-2 of the LHC. Tech. rep. Geneva: CERN, 2015 Nov. Available from: https://cds.cern.ch/record/2064383

40. ATLAS Collaboration. Identification of hadronic tau lepton decays using neural networks in the ATLAS experiment. Tech. rep. Geneva: CERN, 2019 Aug. Available from: https://cds.cern.ch/record/2688062

41. ATLAS Collaboration. Trigger menu in 2018. Tech. rep. Geneva: CERN, 2019 Oct. Available from: https://cds.cern.ch/record/2693402

42. ATLAS Collaboration. Performance of electron and photon triggers in ATLAS during LHC Run 2. Eur. Phys. J. C 2019 Sep; 80:47. 56 p. DOI: 10.1140/epjc/s10052-019-7500-2. arXiv: 1909.00761

43. ATLAS Collaboration. Performance of the ATLAS muon triggers in Run 2. JINST 2020 Apr; 15:P09015. 60 p. DOI: 10.1088/1748-0221/15/09/p09015. arXiv: 2004.13447

44. ATLAS Collaboration. The ATLAS Tau Trigger in Run 2. Tech. rep. Geneva: CERN, 2017 Jul. Available from: https://cds.cern.ch/record/2274201

45. ATLAS Collaboration. Luminosity determination in pp collisions at $\sqrt{s} = 13$ TeV using the ATLAS detector at the LHC. Tech. rep. CERN, 2019 Jun. Available from: https://cds.cern.ch/record/2677054

46. Meyer AB. Physics with LHC Run-3 and HL-LHC. D-CMS Workshop 2019 at KIT. 2019. Available from: https://www.desy.de/~ameyer/fspcms_run3_hllhc_190913.pdf

47. Aker M et al. Direct neutrino-mass measurement with sub-electronvolt sensitivity. Nature Phys. 2022; 18:160–6. DOI: 10.1038/s41567-021-01463-1. arXiv: 2105.08533 [hep-ex]

48. Buonocore L, Nason P, Tramontano F, and Zanderighi G. Photon and leptons induced processes at the LHC. Journal of High Energy Physics 2021 Dec; 2021. DOI: 10.1007/jhep12(2021)073

49. DELPHI Collaboration. Search for doubly charged Higgs bosons at LEP2. Physics Letters B 2003 Jan; 552:127–37. Available from: https://doi.org/10.1016%5C%2Fs0370-2693%5C%2802%5C%2903125-8

50. OPAL Collaboration. Search for doubly charged Higgs bosons with the OPAL detector at LEP. Physics Letters B 2002 Feb; 526:221–32. Available from: https://doi.org/10.1016%5C%2Fs0370-2693%5C%2801%5C%2901474-5

51. L3 Collaboration. Search for doubly-charged Higgs bosons at LEP. Physics Letters B 2003 Dec; 576:18–28. Available from: https://doi.org/10.1016%5C%2Fj.physletb.2003.09.082